AGU PUBLICATIONS

JGR

Journal of Geophysical Research: Atmospheres

RESEARCH ARTICLE
10.1002/2014JD022948

Special Section:
The 2011-12 Indian Ocean Field Campaign: Atmospheric-Oceanic Processes and MJO Initiation

Cloud organization and growth during the transition from suppressed to active MJO conditions

Angela K. Rowe[1] and Robert A. Houze Jr.[1]

[1]Department of Atmospheric Sciences, University of Washington, Seattle, Washington, USA

Abstract During the Dynamics of the Madden-Julian Oscillation/Atmospheric Radiation Measurement Madden-Julian Oscillation (MJO) Investigation Experiment field experiment in the Indian Ocean, the National Center for Atmospheric Research dual-polarimetric S- and Ka-band radar (S-PolKa) radar observed three active Madden-Julian Oscillation (MJO) events. These events were separated by suppressed periods characterized by shallower, more isolated convection and relatively little rainfall. The sensitivity of S-PolKa allowed investigation of the initiation and organization of both nonprecipitating and precipitating clouds. Early in the suppressed periods, shallow nonprecipitating clouds occurred in shear-parallel lines along apparent boundary layer rolls during early morning. Once some of the clouds began to precipitate, small cold pools formed below the showers. By afternoon, the lines all but disappeared with nonprecipitating clouds instead forming along the edges of cold pools. All such convection was limited in depth early in suppressed periods. As the suppressed environment gained moisture, the nonprecipitating clouds were able to grow to larger size, with the deepest precipitating clouds occurring in clusters at intersections of cold pool boundaries by afternoon. Upscale growth into mesoscale convective systems was observed as the suppressed periods transitioned into active MJO phases, contributing to overnight precipitation during the later part of the suppressed period. This study demonstrates the need for models to accurately represent the organization and evolution of nonprecipitating clouds in association with boundary layer dynamics under suppressed conditions of the MJO, prior to the occurrence of precipitating clouds and their cold pools.

Key Points:
- MJO initiation is preceded by nonprecipitating clouds organizing into lines
- Only after nonprecipitating clouds organize do rain cells and cold pools form
- Deep clouds at intersecting cold pools occur late in suppressed periods

Correspondence to:
A. K. Rowe,
akrowe@atmos.uw.edu

Citation:
Rowe, A. K., and R. A. Houze Jr. (2015), Cloud organization and growth during the transition from suppressed to active MJO conditions, *J. Geophys. Res. Atmos.*, *120*, 10,324–10,350, doi:10.1002/2014JD022948.

Received 4 DEC 2014
Accepted 27 AUG 2015
Accepted article online 4 SEP 2015
Published online 9 OCT 2015

1. Introduction

Intraseasonal variability in the tropics is dominated by the Madden-Julian Oscillation (MJO) [*Madden and Julian*, 1971, 1972]. However, MJO forecasting skill is hindered by difficulty in representing all aspects of the convective population and its coupling with the large-scale environment [*Zhang*, 2005], especially over the Indian Ocean. To obtain a better understanding of the development of the convective population over this region, the Dynamics of the Madden-Julian Oscillation (DYNAMO)/Atmospheric Radiation Measurement MJO Investigation Experiment (AMIE) was conducted in the Indian Ocean region as a component of the Cooperative Indian Ocean Experiment on Intraseasonal Variability in Year 2011 [*Yoneyama et al.*, 2013]. Through a comprehensive suite of measurements, including ship- and island-based radars with various frequencies and scanning strategies, a rawinsonde array, shipborne surface flux measurements, and aircraft radar with additional flux observations, the spectrum and evolution of convection was investigated throughout all phases of the MJO. Observational studies using data from this field experiment have described a transition of the precipitating cloud ensemble from one dominated by shallow, isolated convection to a cloud population dominated by clusters of deep convective elements and mesoscale convective systems containing widespread stratiform echo [*Powell and Houze*, 2013; *Zuluaga and Houze*, 2013; *Xu and Rutledge*, 2014]. *Rowe and Houze* [2014] and *Barnes and Houze* [2014] have examined the microphysical nature of the precipitating clouds as observed by the National Center for Atmospheric Research (NCAR) dual-polarimetric S- and Ka-band radar (S-PolKa) during the "active" MJO periods when most of the rainfall occurs.

Between the active MJO periods, "suppressed" conditions prevailed. These suppressed periods were characterized by generally shallower and mostly nonprecipitating convection in a subsidence-dominated, relatively drier large-scale environment [*Johnson and Ciesielski*, 2013; *Powell and Houze*, 2013, 2015; *Ruppert and Johnson*, 2015]. This "preonset" phase of the MJO has been a focal point of research regarding the possible effects of shallow cumulus and moderate cumulus congestus clouds in moistening the environment [e.g., *Benedict and Randall*, 2007; *Hannah and Maloney*, 2011; *Riley et al.*, 2011; *Del Genio et al.*, 2012; *Powell and Houze*, 2013, 2015; *Kumar et al.*, 2014]. A recent study by *Ruppert and Johnson* [2015] suggests that low- to

middle-level moistening is accomplished by relatively shallow clouds that exhibit a pronounced diurnal cycle and marked mesoscale organization in the form of open cells and horizontal convective rolls, as could be seen in coincident satellite and radar data. Throughout these studies, the detailed nature of the nonprecipitating clouds has been largely absent. In this study, the detailed and comprehensive sensing of nonprecipitating clouds provided by the DYNAMO S-PolKa radar observations offers the opportunity to better understand convective initiation along these boundaries preceding the active MJO periods.

Observations from past field projects have shown the important role of environmental shear in the organization and evolution of precipitating convection over the tropical ocean [e.g., *Barnes and Sieckman*, 1984; *LeMone et al*., 1998; *Cetrone and Houze*, 2006]. Active MJO phases during DYNAMO at times exhibited deep convection organized into shear-normal squall lines [e.g., *Rowe and Houze*, 2014; *Barnes and Houze*, 2014]. During suppressed periods, however, deep layer shear was weaker [*Xu and Rutledge*, 2014]. These studies were mostly concerned with shear in a deep tropospheric layer. In order to describe the organization of convection during suppressed periods, the focus turns to the relationship between low-level wind shear and mesoscale organization of shallow clouds (e.g., into lines or open cells) and to the clustering of clouds along cold pool boundaries. A recent study by *Feng et al*. [2015], using DYNAMO/AMIE data and model results to examine cold pools over the Indian Ocean, demonstrated the role of cold pools in triggering subsequent and ever deeper, larger convection. Therefore, cold pools are likely important elements of the buildup of the convective population to one containing deep mesoscale systems during active MJO phases. In another cloud-resolving modeling study, *Schlemmer and Hohenegger* [2014] described an interplay of moisture aggregation and lifting along the edges of cold pools leading to wider, deeper clouds less affected by entrainment. A positive feedback followed in which stronger downdrafts formed from these deeper clouds, leading to a stronger modification of the moisture field favoring further cloud development. In this present study, the complete chain of events is examined, beginning with nonprecipitating clouds forming and organizing prior to the appearance of the first cold pools and ending with a population that includes the deep mesoscale systems that characterize an active MJO period.

The continuous, high-sensitivity S-PolKa data allow investigation of the internal structure of individual clouds, both precipitating and nonprecipitating, and the spatial organization of the cloud population during suppressed and active MJO conditions. This study describes (1) the internal structure and spatial organization of nonprecipitating clouds seen by S-PolKa in the earliest stages of the suppressed periods, (2) the appearance of cold pools on radar and the role they played in the transition toward deeper precipitating convection, and (3) the evolution of the cloud population toward one containing mesoscale convective systems in an active MJO. The capability of S-PolKa for this analysis and the methods applied to the data are described in the section 2. These methods include identification of shallow convective clouds, their internal structure, and their spatial organization in relation to the low-level wind shear. Section 3 describes the manner in which the nonprecipitating cumulus clouds organized upscale and eventually led to a population containing precipitating, cold pool-producing clouds. Section 4 addresses the role of the diurnal cycle in these processes, and section 5 considers the implications of these observations for understanding the MJO.

2. Data and Methods

2.1. S-PolKa Data

NCAR's S-PolKa radar was located on Addu Atoll in the Maldives (0.6°S, 73.1°E) from 1 October 2011 to 15 January 2012. Full 360° azimuthal surveillance scans at eight constant elevation angles from 0.5° to 11.0° were followed by two sectors of range-height indicator scans (abbreviated RHIs, this type of scan is executed by sweeping the antenna beam through a given elevation angle range at a fixed azimuth) within a 15 min scanning cycle. The full volume scans were used to compute precipitating feature statistics in this study, with the lowest elevation scans used for the manual tracking of near-surface boundaries. The RHIs provided better vertical-resolution data recorded in elevation bins of 0.5° up to a maximum elevation angle of 41° over two azimuthal sectors where data were collected at azimuthal intervals of 2°. The azimuth sectors consisted of a broad sector to the northeast (4°−82°), primarily over the ocean, and a narrow sector to the southeast (114°−140°), which included coincident data over the Department of Energy Atmospheric Radiation Measurement Program (ARM) Ka-band ARM Zenith Radar (KAZR) located 9 km from S-PolKa. RHIs are presented in this study to describe finer scale microphysical characteristics of convection.

The NCAR group operating S-PolKa applied advanced techniques to provide a reliable data set with reduced noise. This processing is especially crucial for the present study, which relies on low-power returns at the lowest-elevation angle to investigate boundary layer nonprecipitating echo in addition to the precipitating systems. A particle identification (PID) technique, basically as that described by *Vivekanandan et al*. [1999], was then applied to the S-PolKa data. This algorithm uses the dual-polarized radar signals to determine the most probable microphysical characteristics of the particle population sampled by the radar beam at a particular location. Additional details about quality control of this data set and the PID methodology can be found in *Rowe and Houze* [2014].

2.2. Nonprecipitating Echo

Rowe and Houze [2014] focused on precipitating convection; however, the S-PolKa radar is also capable of observing nonprecipitating shallow clouds. The S-PolKa RHIs over the KAZR site provided a means to evaluate a broader spectrum of clouds in this region. *Feng et al*. [2014] compared data from S-PolKa, KAZR, and the Texas A&M Shared Mobile Atmospheric Research and Teaching Radar C-band scanning radar, also located on the atoll, to quantify the types of clouds that each instrument could observe. They found that KAZR's shorter wavelength provided the best observations of weak reflectivity echo associated with nonprecipitating, shallow clouds. However, KAZR pointed vertically, thus having no ability to assess the spatial organization of the clouds, and the Ka-band wavelength was attenuated in precipitation. With a minimum detectable reflectivity of about −24 and −10 dBZ at a distance of 10 and 50 km, respectively, S-PolKa's S-band wavelength observations could reasonably detect nonprecipitating cumulus clouds (more than 80% of those observed by KAZR) within 30−50 km range. Thus, S-PolKa is the ideal tool to observe both the nonprecipitating population's organization and evolution into a population containing precipitating clouds and was therefore used to assess the horizontal patterning of the shallow nonprecipitating clouds in addition to sensing the precipitating clouds that attenuated the KAZR signal.

Moreover, because of its dual-polarization capability, S-PolKa data provided information on the internal structure of the nonprecipitating clouds that could not be inferred from KAZR. Distinct radar signatures from polarimetric S-PolKa observations of nonprecipitating clouds are shown in Figure 1. The clouds in this example occurred during the early November suppressed period identified by *Rowe and Houze* [2014] (see their Figure 1). The reflectivity (Z) panel shows two distinct layers of echo (one just below 1 km and another near 2−2.5 km in height). These echoes are near the sensitivity threshold and are detections of Bragg scatter resulting from moisture gradients in the atmosphere [e.g., *Davison et al*., 2013]. In their analysis of S-PolKa data from the Rain in Cumulus over the Ocean (RICO) field experiment, *Davison et al*. [2013] related one of the observed Bragg scattering layers (BSLs) to a thin transition between a well-mixed subcloud layer and a less mixed cumulus cloud layer within the overall tropical marine boundary layer. This transition layer typically contained shallow clouds that most likely led to a mix of Bragg and Rayleigh scattering. Applying BSL analysis to the DYNAMO S-PolKa data set, *Davison* [2014] noted transition layers between 0.5 and 1.0 km mean sea level. Therefore, the BSL located just below 1 km in Figure 1 was likely related to such a transition layer. Along this BSL, areas of reflectivity >0 dBZ were observed. These relatively stronger radar echoes were associated with shallow, nonprecipitating clouds along this transition layer. These observations of early echo at S band were similar to those described in studies of shallow cumulus in Florida [*Knight and Miller*, 1998; *Knight et al*., 2002] and of oceanic trade wind cumulus during RICO [e.g., *Knight et al*., 2008; *Snodgrass et al*., 2009; *Minor et al*., 2011]. In these and the present studies, "mantle echoes" with near-zero reflectivity draped over and enveloped the core of the cloud, somewhat like the zone of hot gases around a flame, as a result of Bragg scatter. While it has been noted that Bragg echoes have near-zero differential reflectivity (Z_{DR}) because of turbulent mixing [e.g., *Knight et al*., 2002; *Melnikov et al*., 2011; *Minor et al*., 2011], it is known that spherical cloud droplets also produce near-zero Z_{DR}. The S-PolKa example from DYNAMO/AMIE (Figure 1) shows near-zero Z_{DR} in echoes with reflectivity between 0 and ~7 dBZ. In addition, the S-PolKa dual-polarization data allow these echoes to also be linked to locally reduced values of linear depolarization ratio (L_{DR}) and correlation coefficient (ρ_{HV}) values near 1, providing increased confidence in the identification of small, nearly spherical cloud droplets, as suggested by the PID [e.g., *Straka et al*., 2000].

While the exact delineation between Bragg and Rayleigh scattering can be ambiguous at S band, the ability to identify shallow nonprecipitating cumulus clouds using S-PolKa, and distinguish them from cumulus clouds producing precipitation at the surface, is possible with the dual-polarization capability of this radar.

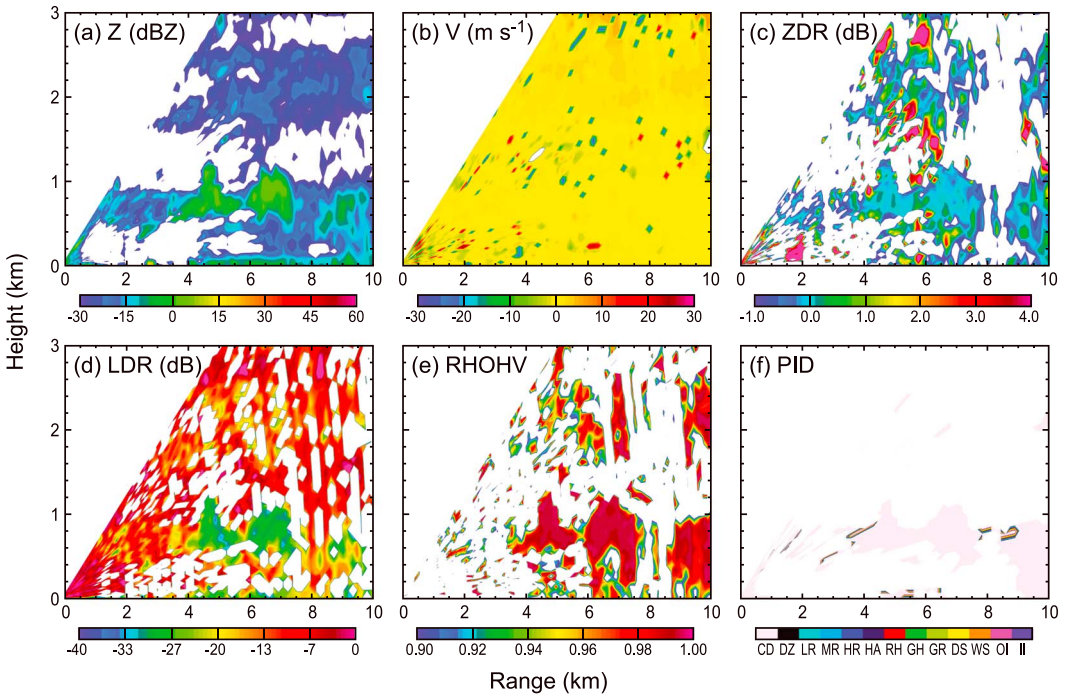

Figure 1. An RHI at 0535 UTC on 6 November 2011 at an azimuth of 45°. Variables are (a) reflectivity (dBZ), (b) radial velocity (m s^{-1}), (c) differential reflectivity (dB), (d) linear depolarization ratio (dB), (e) cross-correlation coefficient, and (f) NCAR's particle identification (PID; CD: cloud droplets, DZ: drizzle, LR: light rain, MR: moderate rain, HR: heavy rain, HA: hail, RH: rain-hail, GH: graupel/hail mixture or rimed aggregates, GR: graupel/rain mixture, DS: dry aggregates, WS: wet aggregates, OI: horizontally oriented small ice crystals, and II: small ice crystals with no preferred orientation).

In the following sections, additional examples will be presented in which nonprecipitating clouds, identified via their polarimetric signatures, appeared before the development of the first precipitating features during the suppressed periods. It will be shown that just prior to the onset of precipitation, these nonprecipitating clouds were observed by S-PolKa to organize into linear or open-cell patterns. The evolution of these cloud patterns including formation of precipitation and subsequent cold pools, which trigger additional convection, will be described in later sections.

2.3. Precipitating Feature Identification

To investigate characteristics of precipitating features during DYNAMO, each S-PolKa volume was gridded to Cartesian coordinates at 0.5 km horizontal and vertical resolution using the NCAR Sorted Position Radar Interpolator [*Mohr and Vaughan*, 1979]. Contiguous areas of gridded reflectivity greater than 15 dBZ at 1 km vertical height were flagged as individual precipitating features; this reflectivity threshold was also used in the *Rowe and Houze* [2014] DYNAMO study. An ellipse-fitting method, described in *Nesbitt et al*. [2006] and applied to DYNAMO S-PolKa data in *Rowe and Houze* [2014], was used to determine the major axis length of each identified precipitating feature. Similar to definitions used in the *Rowe and Houze* [2014] study, a precipitating feature was required to have a major axis of at least 2 km and mesoscale convective systems (MCSs) were defined as those features with a maximum axis length greater than 100 km.

One aim of this study is to determine when the precipitating convection occurred after the nonprecipitating cloud population became organized into lines or open cells. In addition, the upscale growth of convection to MCS-scale features is of interest during the transition from suppressed to active MJO conditions. To help describe this evolution of the precipitating cloud population, a convective-stratiform partitioning algorithm was applied to the reflectivity data. This partitioning allowed for determination of the relative contribution to total rainfall from both the isolated convective features and those embedded within larger systems, as well as from the stratiform component of MCSs. This algorithm is a modified version of the *Steiner et al*. [1995] method, as adapted by *Yuter and Houze* [1997], and was applied to the gridded reflectivity field at the 2.5 km vertical level. Input parameters to this algorithm were tuned for this data set as described in *Powell and Houze* [2013].

The combination of identifying precipitating features stratified into groups of sub-MCS-scale and MCS-scale features, and determining the relative contribution of convective and stratiform components of the precipitating echo, provides a means to describe the evolution of precipitating convective systems during DYNAMO. This additional procedure allows for extension of the descriptions of nonprecipitating echo in earlier stages of the suppressed periods into the MJO onset periods to include when domain-wide precipitation drastically increased and MCSs were a major part of the cloud population.

2.4. Cold Pools

Unlike precipitating features, cold pools could not be tracked using a simple reflectivity threshold. Nonetheless, cold pools appeared as distinctly bounded echo-free regions, allowing for them to be manually tracked in time. The boundary layer over the tropical ocean was turbulent, humid, and consequently characterized by weak echo noise. Small convective features (identified by the method described above) produced cold pools, and the visible manifestation of the cold pool was a "hole" in the background echo detected by S-PolKa low-elevation scans in the environment surrounding precipitating features. These low-level echo-free regions behind gust fronts, generated in regions of downdrafts and rain-cooled air, were likely caused by subsiding air and stabilization, which limits rising thermals [*Wilson et al*., 1994; *Tompkins*, 2001]. *Tompkins* [2001] used modeling to show that a positive anomaly in equivalent potential temperature exists at the boundary of the spreading cold pools, whereas within cold pools, there is a lack of significant humidity and temperature gradients. Moisture gradients between the edges and the surrounding undisturbed boundary layer result in the cold pools being bounded by slightly enhanced radar reflectivity (~0 dBZ) caused by Bragg scattering. Dynamic lifting occurs at the leading edges of cold pools, and enhanced cloud liquid water along cold pool boundaries has been found in observations from RICO [*Li et al*., 2014]. Clouds form atop these moist patches at the leading edges of the cold pools [e.g., *Schlemmer and Hohenegger*, 2014] leading to a localized enhancement of radar reflectivity for a sensitive S-band radar such as S-PolKa.

Due to both Bragg and Rayleigh scattering along these boundaries and variability of boundary layer conditions, the reflectivity enhancement was not always the same so the cold pools were more readily followed manually. Cold pool edges were followed by eye until they merged with nearby boundaries or moved past ~100 km range of the radar, beyond which the radar beam was generally too far above the ground and the beam too wide to see the signature. A similar pattern recognition using S-PolKa observations for manually identifying cold pools was used to describe convection under suppressed conditions over land in Amazonia [*Lima and Wilson*, 2008]. This manual tracking allowed for the horizontal dimensions and lifetimes of cold pools during DYNAMO to be estimated. These characteristics provided a useful comparison to model simulations of cold pool properties by *Feng et al*. [2015]. In that study, 52 cold pools on 10 October 2011 were tracked by the manual method. In this study, the same October case study along with seven additional cases from October, November, and December will be examined.

Ruppert and Johnson's [2015] analysis of S-PolKa and Moderate Resolution Imaging Spectroradiometer data in relation to environmental conditions noted a prominent open cellular cloud structure, similar to that described by *Johnson et al*. [2001] over the western Pacific warm pool, but did not relate these features to cold pools that likely existed within these time periods. To ensure that the ringed boundaries observed in the S-PolKa data presented herein were indeed related to cold pools, each enclosed echo-free region included in this analysis was traced back to a precipitating feature. This connection will be illustrated in examples presented in the following sections. While it is difficult to determine if each individual bounded echo-free hole was related to a temperature depression, those boundaries that passed over surface stations on Gan Island and the R/V *Revelle* were typically associated with temperature drops on the order of 1°C along with increases in water vapor moisture and wind speed [e.g., *Feng et al*., 2015]; therefore, the echo-free holes in the wake of convection will all be referred to as cold pools, keeping in mind that some may have been solely a result of moisture gradients with varying degrees of temperature depressions.

2.5. Wind Shear

To place the spatial patterns of nonprecipitating echoes within the context of low-level wind shear, vertical profiles of zonal and meridional wind components were obtained from the Colorado State University-DYNAMO upper air and surface gridded analyses [*Johnson et al*., 2015]. Observational data sets from DYNAMO, including sounding and dropsonde data, were supplemented by European Centre for Medium-Range Weather Forecasts

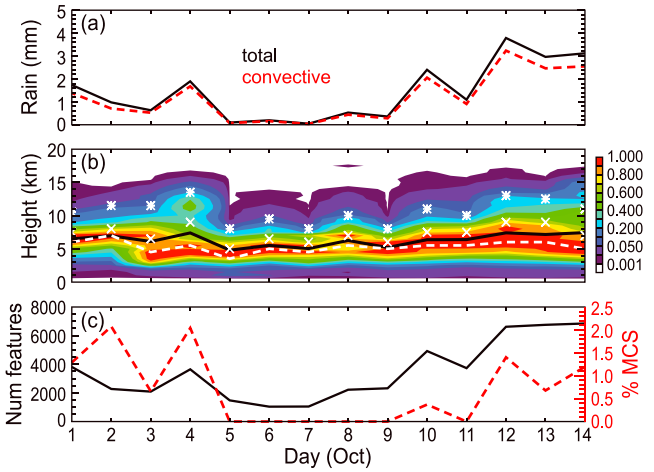

Figure 2. (a) Time series of areal-averaged daily total (black line) and convective (red dashed line) rainfall in millimeter. (b) Time series of daily mean echo-top heights (km; 0 dBZ maximum height) for all feature grid points (black line), of daily 50th (white dashed line), 75th (white crosses), and 95th (white asterisks) percentiles of feature maximum echo-top heights. Color-filled contours are daily echo-top height frequencies for all feature grid points presented as the fraction relative to maximum frequency for the given day. (c) Time series of the number of daily precipitating features (black line) and the relative percentage of those daily features identified as MCSs (red dashed line). Time includes days of the October suppressed period only (1–14 October 2011).

Observational Analyses in data-sparse regions to create fields daily every 3 h on a 1° latitude/longitude grid at 25 hPa vertical resolution using the multiquadric interpolation scheme of *Nuss and Titley* [1994]. This version of the data set (version 3b), as further detailed in the Readme file available at http://johnson.atmos.colostate.edu/dynamo/products/gridded/v3b/Readme-v3b.txt, was used to calculate vertical wind shear within the S-PolKa domain during DYNAMO. Low-level wind shear was determined over 0–1 km, 0–1.5 km, and 0–2 km height levels to account for the height ranges over which nonprecipitating echo was observed within the 150 km range from the radar.

3. The Evolving Boundary Layer Structure and Cloud Population

3.1. October 2011

Time series of S-PolKa areal-averaged daily-accumulated rainfall and MCS coverage presented in *Rowe and Houze* [2014] showed the occurrence of three active MJO periods, each lasting a few weeks beginning around the middle of October, November, and December. During the earlier halves of each month, suppressed conditions prevailed, although with slightly different environmental properties. In this paper, the focus is on these suppressed periods and the manner in which the conditions in each suppressed period evolved up to the time that active conditions were beginning.

S-PolKa was located on the southwest corner of the northern sounding array, in which the sounding heat and moisture budgets showed a preonset (suppressed) MJO stage from 1 to 13 October. This period was characterized by predominant subsidence, with relatively humidity generally less than 50% between the tropopause and 800 hPa [*Ruppert and Johnson*, 2015]. Time series of daily radar-derived quantities during this October suppressed period are presented in Figure 2. Areal-averaged rainfall (total and convective; Figure 2a); normalized frequency of echo-top heights (defined as the maximum height of 0 dBZ reflectivity for each grid point included in all precipitating features, displayed as color-filled contours); the mean echo-top heights for all precipitating grid points (black line); and the 50th, 75th, and 95th percentiles of the maximum echo-top heights identified for individual precipitating features (Figure 2b) are shown here. Figure 2c shows the number of precipitating features identified for each day during this suppressed October period, along with the relative percentages of those features meeting the MCS threshold (100 km major axis). During the first few days of this period, MCS-sized features continued to populate the scene as the environment transitioned into suppressed conditions after the previous active event (not documented by the DYNAMO/AMIE radar or sounding networks). Fifth of October marked the first day of the period in which no MCSs were observed, with coincident reductions in rain, echo-top heights (both for maximum heights of individual features and for all grid points where precipitation was occurring), and overall number of precipitating features.

Figure 3 highlights the evolving organization of clouds over a 2 h period from 0831 to 1046 UTC on this suppressed day. In Figure 3a, a notable observation is the organization of the background reflectivity into lines in the northern half of the domain. *Weckwerth et al.* [1996] showed that boundary roll circulations can create localized lines of moisture convergence and upward air motion. The enhanced water vapor content and vertical velocity along the lines promote an extension of the boundary layer moisture into the relatively drier free

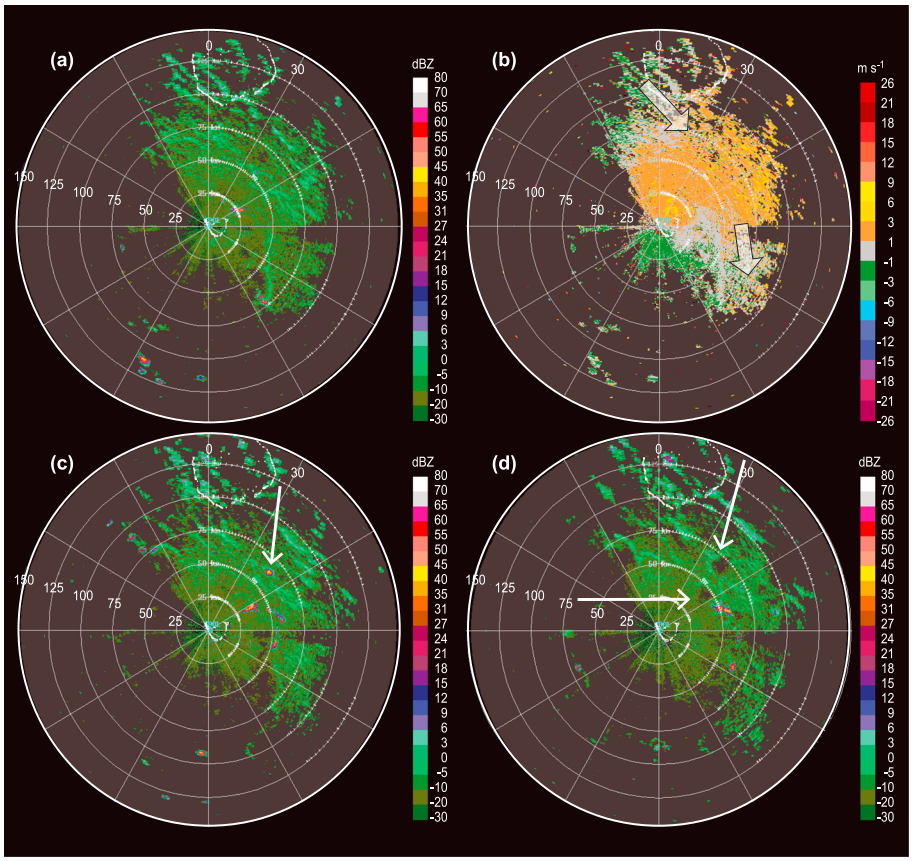

Figure 3. A series of S-PolKa surveillance scans at 0.5° elevation angle from 5 October 2011 showing (a) reflectivity at 0831 UTC, (b) radial velocity at 0831 UTC, (c) reflectivity at 0931 UTC, and (d) reflectivity at 1046 UTC. Each concentric circle marks 25 km range rings from the radar, with the maximum range shown of 150 km. Azimuthal angles are divided into 30° sectors starting clockwise from 0° due north of the radar. The white tick marks indicate location of all RHIs. Cool (warm) colors in Figure 3b indicate radial velocities toward (away from) the radar. The block arrows in Figure 3b indicate the direction of the 0–2 km wind shear vectors at 0900 UTC. The solid white arrow in Figure 3c, and throughout all figures, points to specific echo and echo holes described in the text.

troposphere above and can lead to convective initiation. The lines described here are consistent with the presence of such rolls.

Previous studies have suggested a minimum wind-speed criterion for these rolls to exist [e.g., *Kuettner*, 1959, 1971; *Weckwerth et al*., 1997]; however, *Weckwerth et al*. [1999] noted that this value could be very small (i.e., mean convective boundary layer wind speed ~2 m s^{-1} or 10 m altitude wind speed of ~1 m s^{-1}). Corresponding radial velocity data at this time (Figure 3b) show that in the vicinity of the rolls to the north and east of the radar, the flow was about 2–3 m s^{-1}. Near S-PolKa, the low-level flow shown by the Doppler velocity field (Figure 3b) was out of the south-southwest, consistent with south-southwesterly winds observed near the surface in the Gan sounding at 0900 UTC on this day (not shown). Winds veered to nearly westerly throughout the lowest kilometer at Gan. The radial velocity data observed at the 0.5° elevation angle in the northern part of the domain show a similar shift in the winds to southwesterly with distance (and therefore height), indicating that these boundary layer rolls were oriented nearly perpendicular to the flow (Figures 3a and 3b). A 3 h loop of the radar data at this time (not shown) confirmed that these lines were being advected toward the northeast by the low-level winds. Previous studies [e.g., *Kuettner*, 1959, 1971; *Kuo*, 1963; *Asai*, 1970a, 1970b, 1972] noted that the orientation of such cloud lines was not determined by wind direction but rather by the wind shear, with the lines typically oriented nearly parallel to the low-level wind shear direction. A look at the low-level vertical wind shear at this time (Figure 4a) indicates that despite being oriented perpendicular to the wind direction, these rolls located beyond 100 km from S-PolKa were oriented nearly parallel to the 0–2 km wind shear direction, as expected from the classical studies mentioned

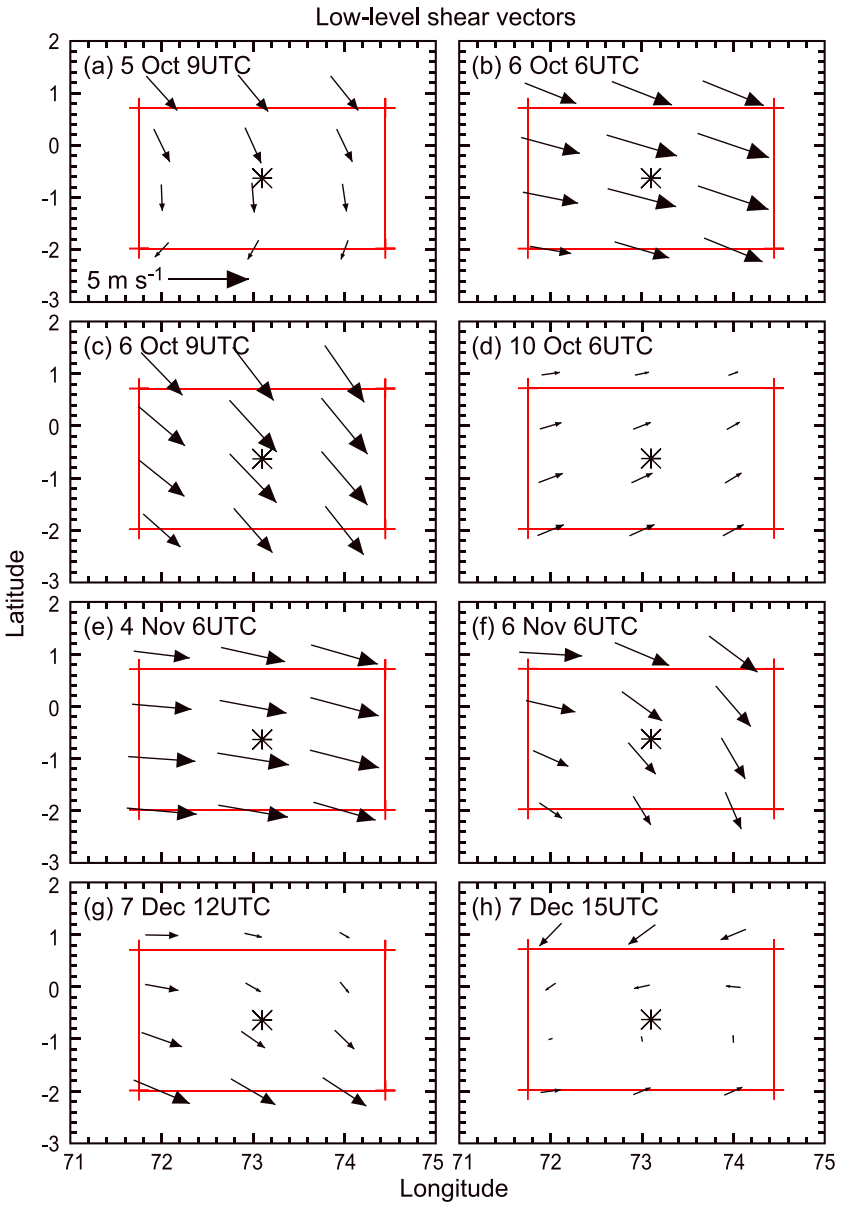

Figure 4. Wind shear vectors are displayed for vertical layers of (a) 0–2 km at 0900 UTC 5 October 2011, (b) 0–1.5 km at 0600 UTC 6 October 2011, (c) 0–1.5 km at 0900 UTC 6 October 2011, (d) 0–1.5 km at 0600 UTC 10 October 2011, (e) 0–1.5 km at 0600 UTC 4 November 2011, (f) 0600 UTC 6 November 2011, (g) 1200 UTC 7 December 2011, and (h) 1500 UTC 15 December 2011. The red boxes indicate the approximate S-PolKa domain (150 km range), and the asterisk indicates the location of S-PolKa. In Figure 4a, the reference vector is plotted, showing the length associated with (5 m s^{-1})/2 km in Figure 4a and (5 m s^{-1})/1.5 km for the remainder of the panels.

above. The wind shear direction shifted to north-northwest to the east of the radar, where a north-south oriented cloud line was also oriented parallel to the wind shear (Figure 3b). The magnitude of the wind shear was low, approximately 0.001–0.002 s^{-1} in the vicinity of the rolls, similar to observations of rolls described by *Weckwerth et al.* [1997] in conditions of very low shear over the convective boundary layer (0.002 s^{-1}).

Later, at 0931 UTC (Figure 3c), a precipitating feature with maximum $Z > 35$ dBZ was observed in the northeast sector, roughly 65 km from S-PolKa. This feature had formed from a cloud located along one of the lines of otherwise nonprecipitating cumulus. An echo-free hole was left after the precipitating convective feature disappeared at 1046 UTC (Figure 3d). The hole was bounded by slightly enhanced reflectivity, which was accounted for by the PID's diagnosis of nonmeteorological echo and cloud droplets owing to Bragg

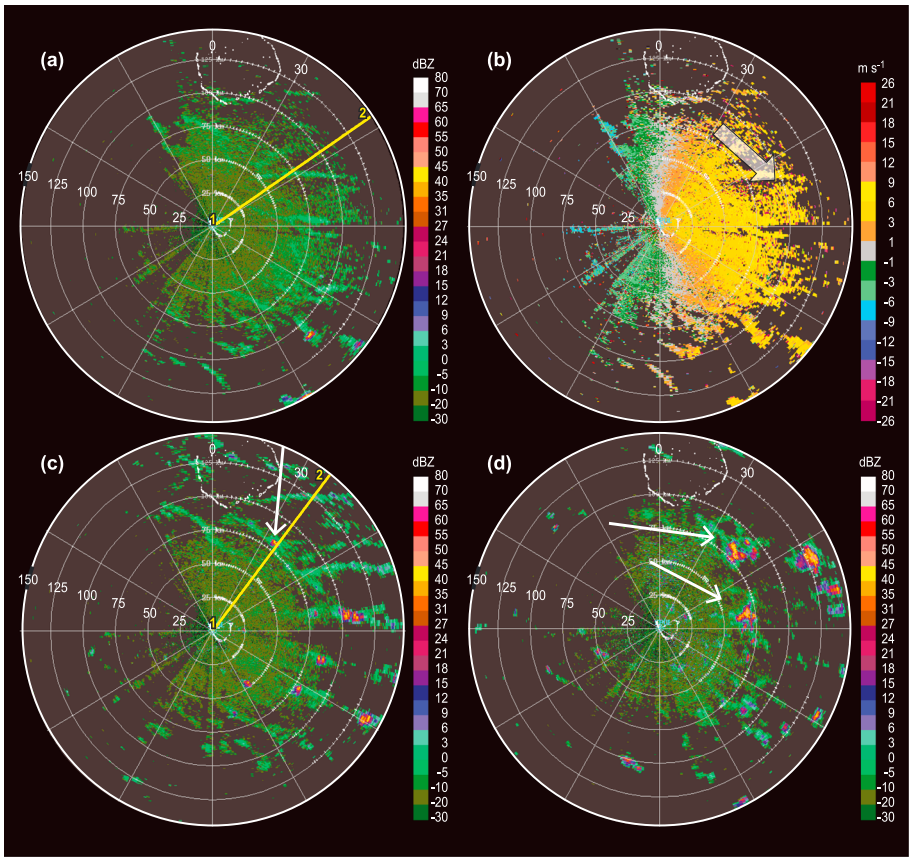

Figure 5. A series of S-PolKa surveillance scans at 0.5° elevation angle from 6 October 2011 showing (a) reflectivity at 0901 UTC, (b) radial velocity at 0901 UTC, (c) reflectivity at 1116 UTC, and (d) reflectivity at 1416 UTC. The yellow lines in Figures 5a and 5c show the locations of the RHIs in later figures. The range rings and tick marks are the same as in Figure 3. The block arrow in Figure 5b indicates the direction of the 0–1.5 km wind shear vector at 0900 UTC. The white arrows in Figures 5c and 5d point to cells and echo-free holes, respectively, that are described in the text.

scatter and shallow, nonprecipitating clouds, respectively. A similarly bounded echo-free hole located to the southwest of this hole was associated with another precipitating convective feature. This pattern recognition exemplifies our method of identifying and tracking cold pools in the S-PolKa data set.

At times when environmental conditions were especially dry (relative humidity $< 50\%$) above the ever-present moist lower levels during this early suppressed period, development of deeper precipitating convective cells was rare. The time series (Figure 2) shows that the general trend of fewer relatively shallow convective features per day continued for several days. An example of convection at 0901 UTC on 6 October (Figure 5a) reveals clearly defined cloud lines on this day. An RHI through one of these lines at this time (Figure 6) shows mantle-cloud signatures of shallow, nonprecipitating convection like those seen in Figure 1. Similar to that previous example, localized concurrent regions of Z~5 dBZ, near-zero Z_{DR}, low L_{DR} (~−25 dB), and ρ_{HV} approaching 1 indicate a mantle caused by nearly homogeneous, nearly spherical cloud-sized droplets. The lines of nonprecipitating clouds in this example extended almost to the eastern edge of the radar domain (Figure 5a). Upward curving and widening of the beam prevented observations of this echo farther from the radar. However, satellite imagery presented by *Ruppert and Johnson* [2015] indicated that these cloud streets existed over a broader area, at horizontal distances beyond S-PolKa's range. In both data sets, these parallel lines were inferred, again, to be horizontal patterns of convective boundary layer rolls.

Low-level wind speeds in excess of 5 m s^{-1} on this day (Figure 5b) supported the favored conditions for boundary layer rolls [e.g., *Weckwerth et al.*, 1997]. Unlike the previous day (Figure 3), these lines were aligned parallel to the flow in the eastern half of the domain (Figure 5b), with winds generally out of the west throughout the boundary layer. The 0–1.5 km vertical wind shear vectors at this time (Figure 4c) were

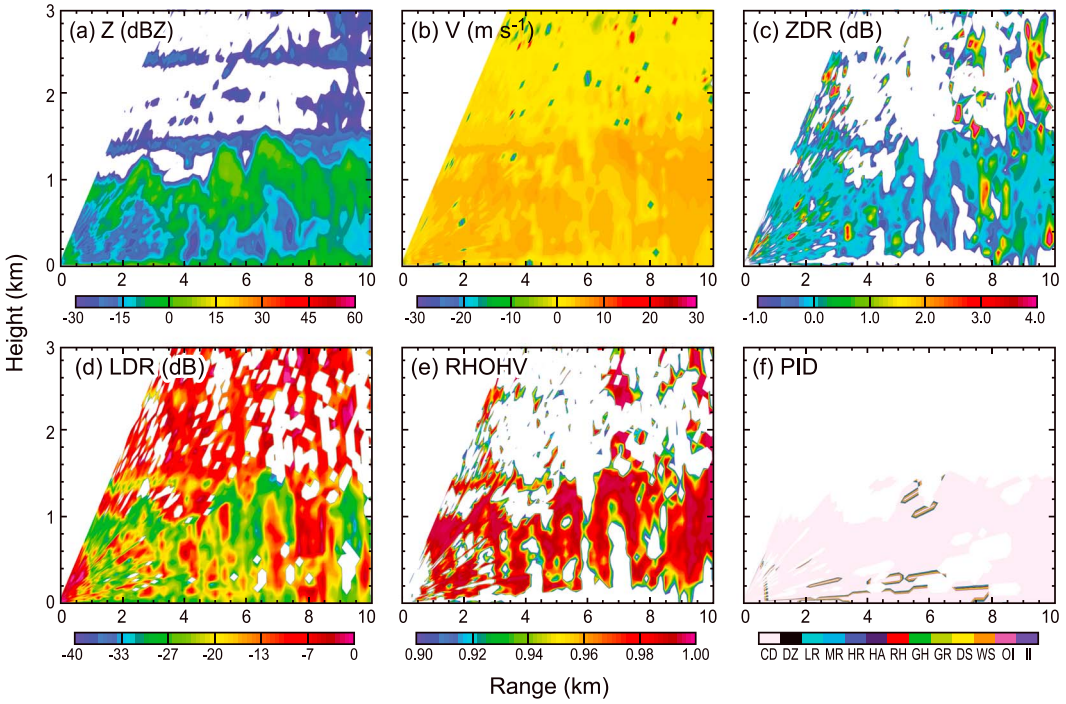

Figure 6. (a–f) Same as in Figure 1 except for 0905 UTC on 6 October 2011 at an azimuth of 56°. The location of this RHI is shown as a yellow line in Figure 4a.

oriented nearly perpendicular to west-east oriented lines. However, when the lines formed several hours earlier, they were oriented nearly parallel to the wind shear direction (Figure 4b), as was the case on the previous day. Note that additional rolls were forming at 0900 UTC (Figure 5a) with a northwest to southeast orientation parallel to the shear (Figure 4c).

Precipitating convective features formed along these rolls (Figure 5c)—both along the older rolls to the east extending toward the edge of the domain and along those oriented parallel to the wind shear direction. Data presented in *Weckwerth* [2000] showed that precipitating convection initiation along boundary layer rolls was possible when the roll depth was nearly equal to the level of free convection (LFC). Sounding data from Gan indicated that the LFC lowered from 771 hPa at 0900 UTC to 835 hPa at 1200 UTC (not shown), placing the LFC below ~2 km. By looking for the presence of these parallel bands at various elevation angles from S-PolKa while considering the height of the beam above the ground, it was determined that they extended in height to at least 2 km. While this is a rough estimate, roll depth is a possible explanation for the precipitating features that initiated along these lines east of the radar by 1116 UTC on 6 October (Figure 5c). Not all of the shallow clouds along these lines, however, grew into precipitating convection. The exact mechanisms responsible for the initiation of each of the precipitating convective features at this time are difficult to discern given the available data sets. However, note in the northeast portion of the domain where precipitating features appeared to be forming at the intersections between the west-east oriented wind-parallel lines and those offset at ~130° that were parallel to the wind shear. These precipitating features may have initiated because of the enhancement of upward motion along the intersection between boundaries. For example, *Wakimoto and Atkins* [1994], in an analysis of sea breeze events, noted cloud development along the intersection points of horizontal convective rolls and the sea breeze front.

Figures 7a and 7b show cross sections through the precipitating feature to the northeast of S-PolKa near 80 km range. Relatively shallow convection, barely reaching 6 km height, must have been dominated by warm-rain processes; most echo remained beneath the melting level, and no ice was identified by the PID. As seen in the time series (Figure 2), mean echo-top heights for all precipitating grid points (black line) and the 50th percentile of feature echo-top heights (white line) were around the melting level on this day (6 October), indicating that this was a typical precipitating feature on this day. While some echo within features extended into the high troposphere on 6 October, the 95th percentile of echo-top heights for features

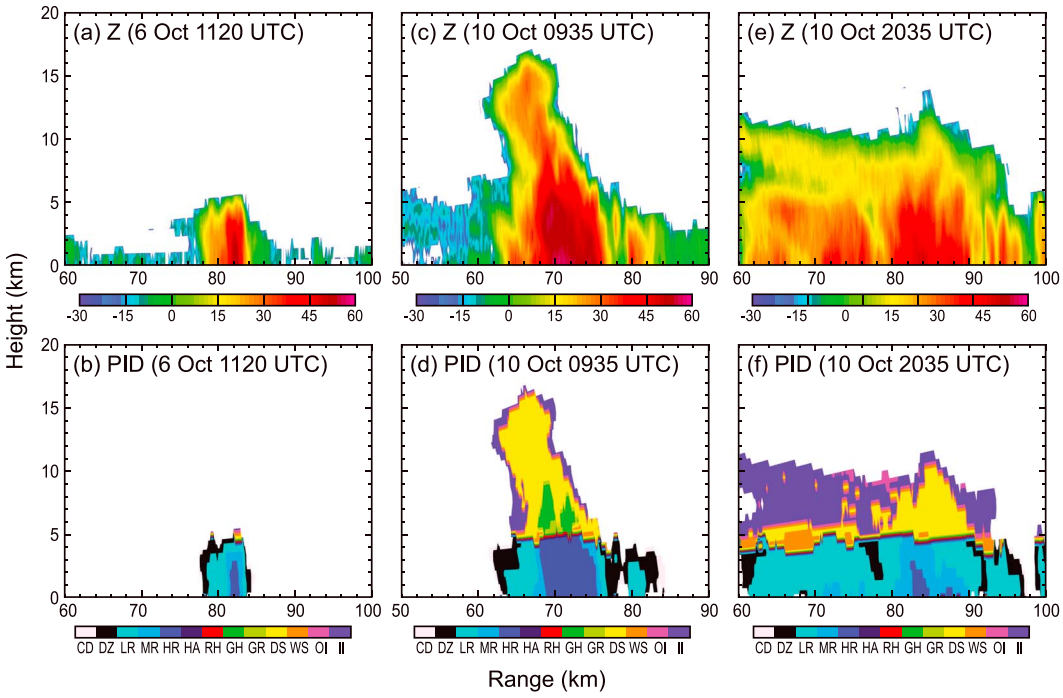

Figure 7. RHIs of convection for 1120 UTC on (a and b) 6 October 2011 at 38° azimuth, (c and d) 0935 UTC on 10 October 2011 at 74° azimuth, and (e and f) 2035 UTC on 10 October 2011 at 122° azimuth showing reflectivity in Figures 7a, 7c, and 7e and the particle identification in Figures 7b, 7d, and 7f. Definitions of the hydrometeor abbreviations are as described for Figure 1.

was relatively low on this day compared to later in this time period. Despite the relatively lower echo-top height, the convective feature in Figures 7a and 7b was clearly precipitating heavily—reflectivities exceeded 50 dBZ and the PID indicated heavy rain. Once having precipitated, these convective features produced trackable cold pools, likely because of downdraft subsidence and advection of drier air from above, as shown in cases of shallow precipitating cumuli during RICO [*Zuidema et al*., 2012]. Several hours later (Figure 5d), these cold pools contributed to the echo-free holes surrounded by cloud rings, later replacing the lines of nonprecipitating clouds that had previously dominated the radar domain.

Following the extremely dry conditions early in the suppressed period, a substantial shift toward increased rainfall occurred. Deeper and more numerous convective features appeared after 9 October; some meeting the 100 km MCS threshold (Figure 2). *Powell and Houze* [2013] and *Ruppert and Johnson* [2015] noted a slight increase in the depth of moistening of the lower troposphere starting around 9 October coincident with this deepening of convective clouds. By early afternoon on 10 October (Figure 8a), the S-PolKa domain was populated by scattered precipitating convection forming on the boundaries of the cold pools left behind by previous precipitating features. Convective boundary layer rolls described in the previous examples were not observed earlier on this day, possibly because of the overall relatively weaker wind shear (Figure 4d) compared to the same time on previous days. While some of these new convective features quickly decayed, leaving behind cold pools of their own, others persisted and intensified over the next several hours, especially those forming along intersecting boundaries (Figure 8b). An RHI through one particularly persistent sub-MCS feature that occurred at this time along intersecting boundaries (Figures 7c and 7d) shows an example of exceptionally deep convection. Echo-top heights extended above 15 km in this convective feature, highlighting the upper extent of depths reached on this day that were absent earlier in the suppressed period (Figure 2). Precipitation-sized ice in the form of graupel reached several kilometers above the melting level, indicating strong updrafts within these deeper, yet still relatively isolated sub-MCS convective features.

A snapshot from S-PolKa later (1216 UTC) on this day (Figure 8c) highlights the continued formation of numerous precipitating features, with many having initiated on intersecting cold pool boundaries. Further depiction of the evolution of this scene, including the production and merger of a selection of these cold

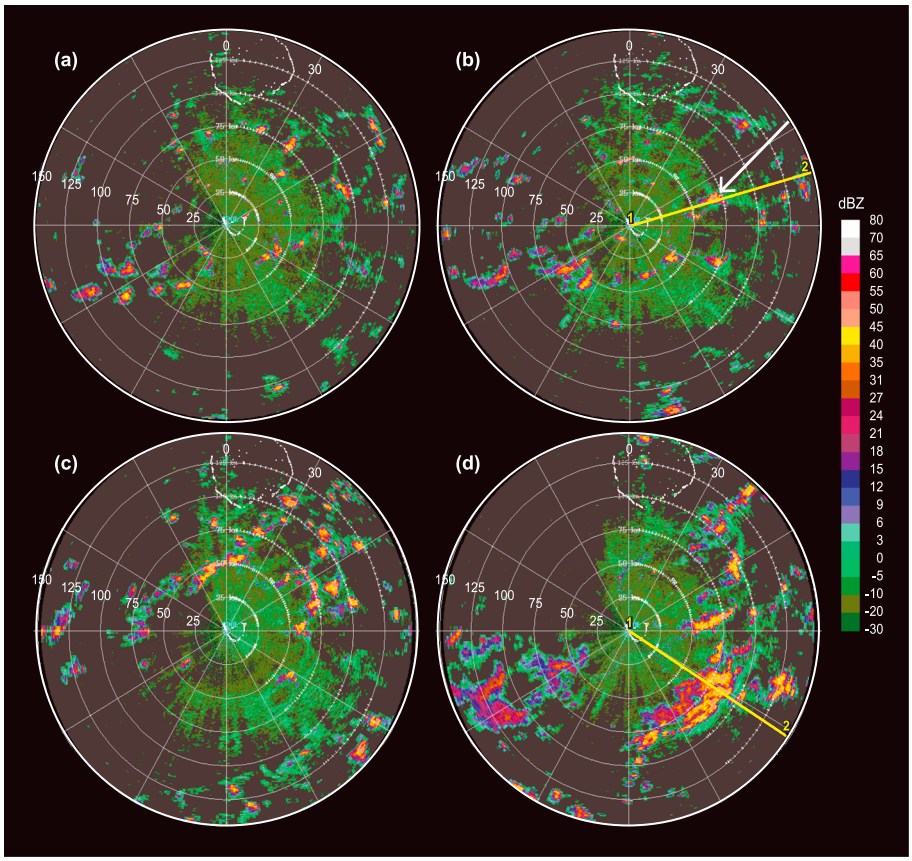

Figure 8. A series of S-PolKa surveillance scans of reflectivity at 0.5° elevation angle from 10 October 2011 at (a) 0746 UTC, (b) 0931 UTC, (c) 1216 UTC, and (d) 2031 UTC. The range rings and tick marks are the same as in Figure 3. The yellow lines show the locations of the RHIs in Figures 6c–6f. The white arrow points to a cell of interest described in the text.

pools, can be seen in Figure 1 of *Feng et al.* [2015]. As suggested by both the time series (Figure 2) and this sequence of images from 10 October (Figure 8), it can be inferred that the production of cold pools contributed to the initiation of numerous new convective features, particularly when these cold pools merged. The high-resolution Weather Research and Forecasting model run described in *Feng et al.* [2015] simulated properties of cold pools that were comparable to those estimated by the manual S-PolKa tracking algorithm used herein and from observations aboard the R/V *Revelle* during DYNAMO. According to their model results, the intersecting cold pools lasted longer, reached deeper, and triggered 73% more convective cells compared to isolated cold pools. Furthermore, they concluded that the initiation of numerous convective cells by these intersecting cold pools reduced the spacing between the convection. This process created larger cloud clusters that limited the amount of entrainment of dry environmental air and allowed the clusters to grow deeper.

On 10 October, not only were the convective features more numerous and deeper than earlier in the month but the convection also clustered into larger features later in the day (Figure 8d). Such clustering behavior was also noted in the model results of *Feng et al.* [2015]. An RHI through this system to the SE (Figures 7e and 7f) shows deep echo reaching 12 km (at approximately the 95th percentile of feature max echo-top heights on this day) and upscale growth into mesoscale entities. This system continued to increase in horizontal extent, later including a stratiform component signaled by a layer of wet aggregates concentrated near the melting level under a deeper layer of small ice crystals aloft. Statistics of the overall hydrometeor profiles in both smaller systems in suppressed periods and MCSs during the active period were presented in *Rowe and Houze* [2014]. The hydrometeor structure shown here is consistent with and representative of those statistical results.

Powell and Houze [2013] also noted that clustering of precipitating echoes was occurring by 12 October, with convective elements and small, lightly precipitating stratiform areas surrounding them, similar to that shown

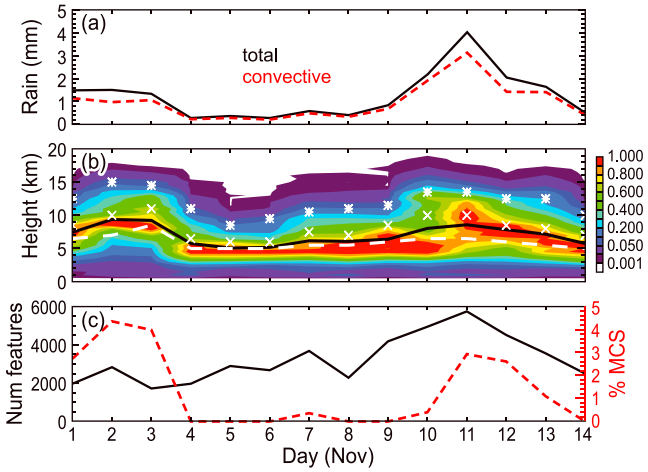

Figure 9. (a–c) Same as in Figure 2 except for the November suppressed period (1–14 November).

in Figures 7e and 7f. This transition is reflected in the October time series (Figure 2). Total rainfall increased with a slight decrease in the relative contribution from convective rainfall, owing to the presence of stratiform precipitation within the small MCSs that appeared more prominently at this time. The upper limit of echo-top heights increased, as did the overall number of precipitating features, including the relative percentage of those features reaching MCS size, near the beginning of the active period on 14 October. Characteristics of the MCSs observed by S-PolKa that followed in the active periods have been described in *Zuluaga and Houze* [2013], *Rowe and Houze* [2014], and *Barnes and Houze* [2014]. The focus of this study is on convection in the suppressed periods leading up to deeper convection.

During mid-October, compared to earlier in the month, cold pools played an important role in initiating new convection and increasing the vertical and horizontal spatial extent of convection, thus contributing to the transition from shallow clouds earlier in the day to deep, mesoscale convective systems characteristic of the active period. It should be noted, however, that cold pool triggering, while an important part of the evolution of the convective population, required prior existence of precipitating features. The organization of nonprecipitating convective clouds in connection with boundary layer rolls promoted the formation of the first precipitating cells. The earlier nonprecipitating cloud organization is thus seen to be an important factor in the transition to the active MJO convective cloud ensemble. The sequential behavior seen here in October occurred again during the lead up to the second (November) MJO event of the DYNAMO/AMIE time period.

3.2. November 2011

Ruppert and Johnson [2015] noted dry conditions (relatively humidity less than 50%) above the near-surface moist layer during the early half of November, similar to the October suppressed period. However, in contrast to the gradual moistening during October, low- to middle-tropospheric moistening took place more quickly so that from early November there was a persistent period of relatively moist conditions. In addition, the mid-tropospheric dry layer only extended down to 550 hPa, compared to 800 hPa during the October suppressed period [*Ruppert and Johnson*, 2015]. Despite these differences, time series of S-PolKa-observed precipitating feature properties during November (Figure 9) show minima in areal-averaged daily rainfall and echo-top heights during the early suppressed period (4–6 November), similar to those in the early October suppressed period (5–7 October), with increases in rain, depth, and number of precipitating features during the latter half of the suppressed period. Note, however, that there were differences in the upper end of echo-top heights compared to October. There was a tendency toward deeper echo during November, possibly a consequence of the deeper moist layer. The maximum in number of individual features was slightly greater during October compared to the maximum for November, while a greater percentage of those features surpassed the MCS threshold in November, although the number of MCSs was still relatively small compared to the total number of features observed.

To compare these time periods in more detail, examples for November are drawn from the most suppressed days of the month (4–6 November) and the day with coincident maxima in rain, depth, and number of precipitating features (11 November), according to the time series in Figure 9. Figure 10 shows PPIs over several hours on 4 November, when these defined characteristics were at a minimum. Similar to the early October examples (Figures 3 and 4), the boundary layer early on 4 November included clouds organized into lines. Small convective features initiated along one of these lines to the northeast by 0531 UTC (Figure 10a) that was oriented parallel to the flow (Figure 10b) and nearly parallel to the wind shear direction at this time

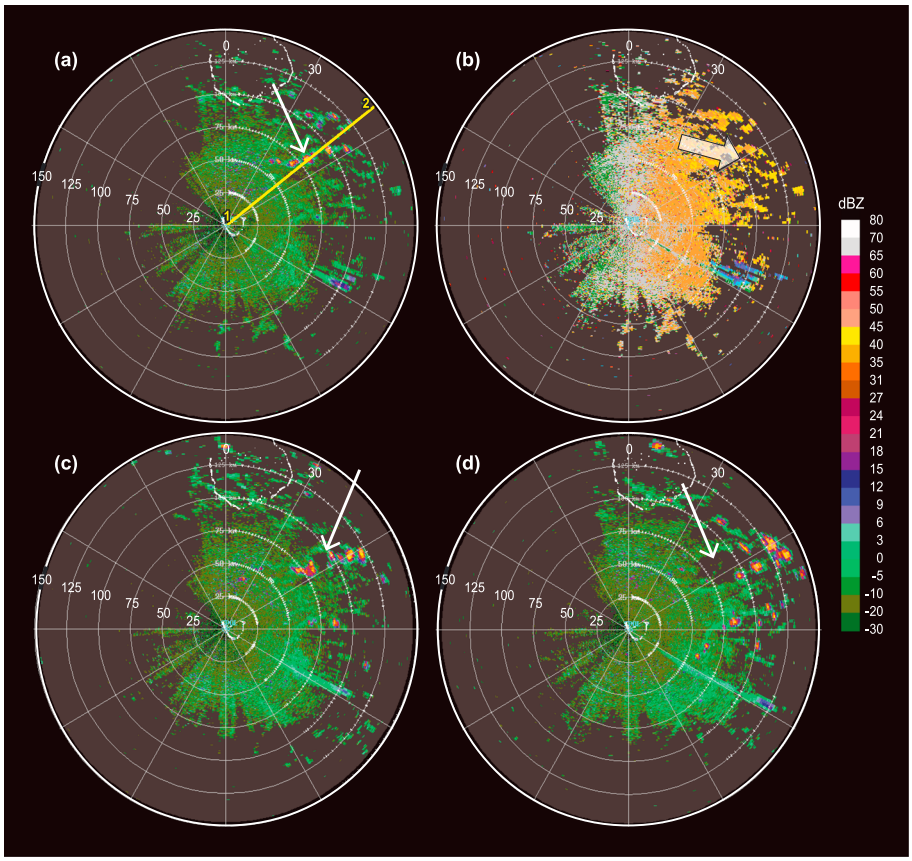

Figure 10. Similar to the October surveillance figures (e.g., Figure 3) except for 4 November 2011 with (a) reflectivity at 0531 UTC, (b) radial velocity at 0531 UTC, (c) reflectivity at 0631 UTC, and (d) reflectivity at 0731 UTC. The yellow line in Figure 10a shows the location of the RHI in Figures 10a and 10b through the cell indicated by the white arrow. The white arrows in Figures 10c and 10d note echo-free holes described in the text. The block arrow in Figure 10b indicates the direction of the 0–1.5 km wind shear vector at 0600 UTC.

(Figure 4e). This observation again highlights the importance of boundary layer rolls in focusing moisture within this relatively drier environment and forcing the moist air to its LCL, which was around 922 hPa (~780 m) at Gan at 0600 UTC. An RHI through one of these precipitating features at this time (Figures 11a and 11b) shows echo tops barely exceeding the melting level, typical of this and other early suppressed days, with a dominance of warm-rain processes corroborated by the PID; the vertical echo growth was likely limited because of the relatively drier air aloft via entrainment. As in the early October case, these relatively shallow precipitating clouds left behind cold pool footprints, seen as an echo-free hole in the northeast quadrant in Figure 10c, contributing to the decrease in parallel line patterns by the afternoon (Figure 10d).

The cloud lines observed early on 4 November were not as clearly defined on other days during the most suppressed November time period. A PPI from 0601 UTC on 6 November (Figure 12a) shows a general lack of widespread linear organization of the nonprecipitating clouds. One line of clouds was evident to the north-northeast of the radar at this lowest-elevation scan (Figure 12b), oriented nearly parallel to the low-level wind shear direction at this time (Figure 4f). Although wind shear magnitudes were similar on this day to previous days when numerous, persistent boundary layer rolls were observed, the difference between this scene and those previous cases may be because of weaker winds. In their analysis of flux measurements from the R/V *Revelle* and data from the greater sounding array, *Ruppert and Johnson* [2015] noted conditions more favorable for rolls during the October suppressed period and open cells during November because of overall weaker low-level winds throughout the November suppressed period compared to October. This difference can also be seen in the radial velocity data in this example, which had velocities generally $<5\ \mathrm{m\ s^{-1}}$ compared to slightly stronger radial velocities observed on 6 October. This relationship between wind and boundary layer organization is consistent with the results described in the *Weckwerth et al.* [1999] analysis

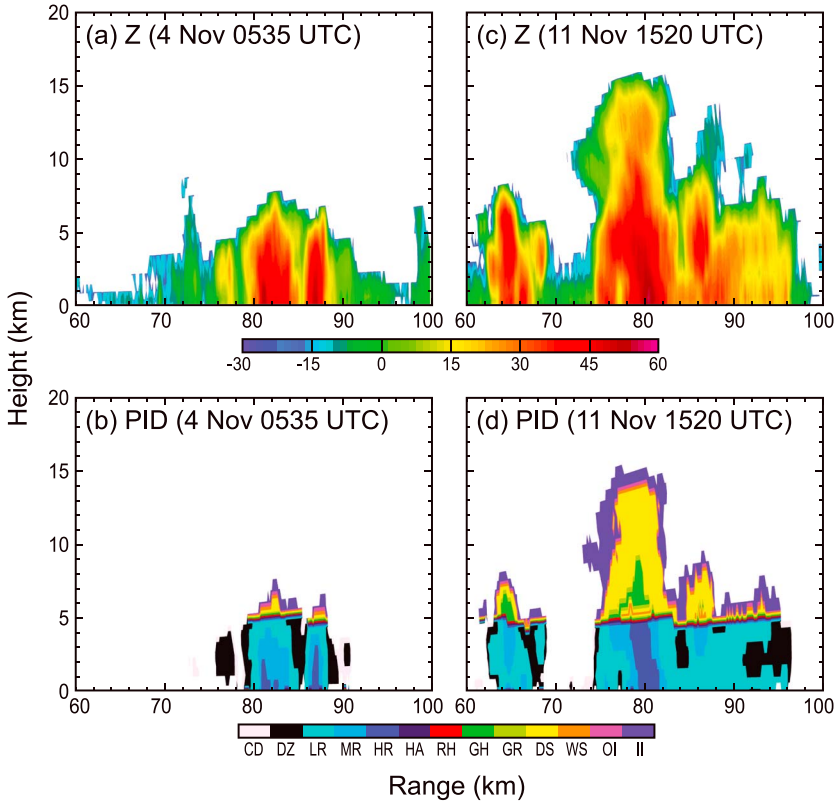

Figure 11. RHIs through cells at (a and b) 52° azimuth at 0535 UTC on 4 November 2011 and at (c and d) 52° azimuth at 1520 UTC on 11 November 2011. Reflectivity is shown in Figures 11a and 11c, and particle identification results are presented in Figures 11b and 11d. Particle categories are as described in Figure 1.

of horizontal convective boundary layer rolls and suggests a dominance of open cells rather than lines in this scenario. Several hours later, scattered isolated precipitating features developed in this suppressed environment, including one forming at the intersection of two open cells (Figure 12c). While remaining relatively shallow, it appears that this precipitating feature was capable of producing a cold pool. However, with the prevalence of open cells in the vicinity of the precipitating features in this example (Figure 12d), it was more difficult to distinguish cold pools from open cells. Nevertheless, it was evident that subsequent formation of precipitating features diminished as the day progressed, similar to examples from the early October suppressed period.

Shifting attention forward to 11 November, the day of peak rainfall, it is evident that mean echo-top heights, number of precipitating features, and MCSs were similar to those in the latter half of the October suppressed period. A group of precipitating convective features was present at 1346 UTC in the northeast quadrant of the domain (Figure 13a), while more widespread precipitation echo had moved into the domain from the southwest. In the northeastern sector, increased clustering of convection was evident at 1446 UTC (Figure 13b) and persisted until 1516 UTC (Figure 13c), leaving behind a cold pool (see arrow). Such clustering into larger, more persistent convective systems is consistent with the *Feng et al*. [2015] analysis, which found reduced spacing between rain cells and deeper convection initiating along intersecting cold pool boundaries compared to rain cell formation at the edges of isolated cold pools. An RHI through this growing precipitating feature (Figures 11c and 11d) shows echo extending above 15 km, exceeding the 95th percentile for maximum feature echo-top heights on this day. The PID-inferred graupel reached heights of nearly 10 km and extended over a greater horizontal area. The continued upscale growth of this precipitating convective feature into a small MCS into the night was evident at 1646 UTC (Figure 13d). An increase in stratiform echo was reflected in the relatively lower contribution of convective rainfall to overall rain on this day (Figure 9). These examples further support the idea that despite differences in the October and November suppressed periods' initial boundary layer structures and rates of moistening, the subsequent development

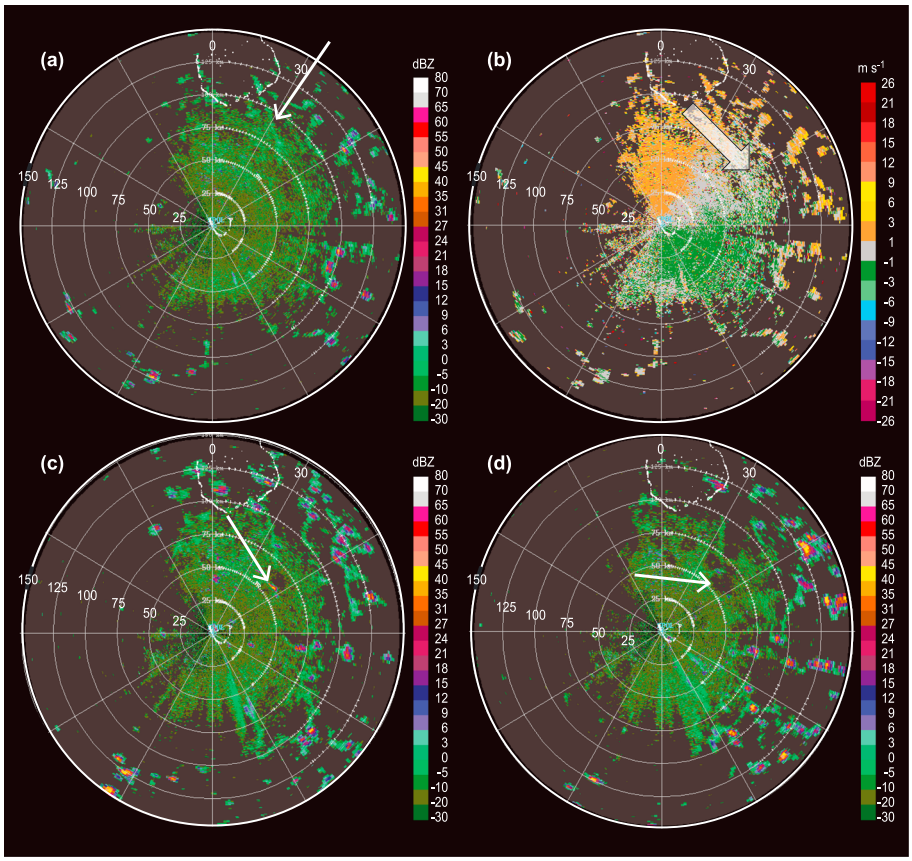

Figure 12. Similar to Figure 3 except for 6 November 2011 with (a) reflectivity at 0601 UTC, (b) radial velocity at 0601 UTC, (c) reflectivity at 0746 UTC, and (d) reflectivity at 0946 UTC. The white arrow in Figure 12a points to a line of clouds described in the corresponding text, Figure 12c to a precipitating cell, and Figure 12d to an echo-free hole. The block arrow in Figure 12b shows the direction of the 0–1.5 km wind shear vector at 0600 UTC.

and organization of precipitating convection by intersecting cold pools was similar during the transition to the active phases in both months.

3.3. December 2011

December over the Indian Ocean was not characterized by the prototypical MJO development that was observed during October and November [*Gottschalck et al.*, 2013]. The "mini-MJO" event of December, as described in *Gottschalck et al.* [2013], shared dynamical characteristics with the previous two events but displayed a less coherent signal in terms of smaller anomalies in 200 hPa velocity potential and a less clear eastward propagation in the outgoing longwave radiation. Despite the conflicting factors associated with this event, a period of suppressed conditions occurred after the November active period followed by enhanced convection in December at a time of strong low-level westerly wind anomalies. Within this different large-scale environment, *Rowe and Houze* [2014] showed that statistics of the microphysical aspects of the convection during December quantitatively differed from those of the October and November active periods, although they were qualitatively similar in terms of the vertical distribution of hydrometeor types. Therefore, the behavior of convection leading up to the active period of December is not necessarily expected to be similar to the more typical MJO initiations of October and November. Nevertheless, the nonprecipitating phase of the December convective buildup was similar to the other months. This similarity will be demonstrated in the following examination of the S-PolKa-observed convective events.

Figure 14 shows the time series of areal-averaged daily rainfall, daily echo-top heights (mean and frequencies for all feature grid points and percentiles of maximum values for individual features), and number of identified precipitating features, including those surpassing the MCS threshold, in December. While this month began with higher values of these quantities, as the environment transitioned out of the previous active

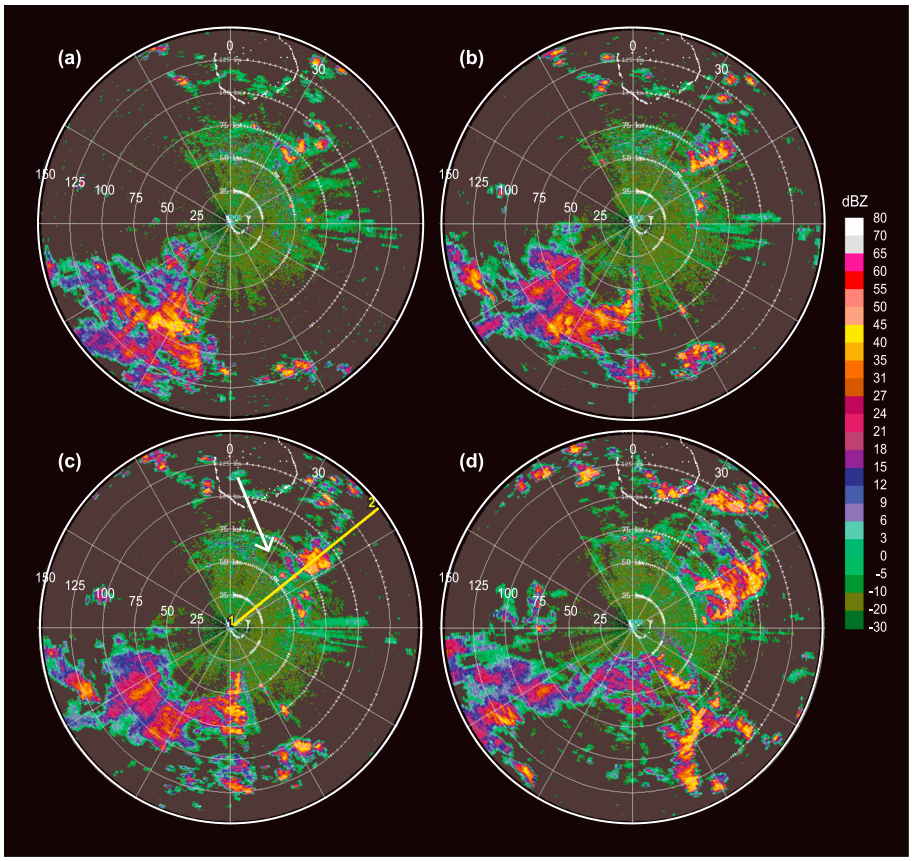

Figure 13. Same as in Figure 3 except for 11 November 2011 at (a) 1346 UTC, (b) 1446 UTC, (c) 1516 UTC, and (d) 1646 UTC. The yellow line in Figure 13c indicates the location of the RHI in Figures 10c and 10d.

phase, the minima in these values were generally restricted to only 2–3 days. This pattern was similar to October and November except that it occurred over a shorter time period than the most suppressed days of the previous two events. The rapid increase in rainfall, including increases in the contribution from stratiform precipitation, number of precipitating features, and percentage of MCSs, occurred over a shorter time period than that separating the October and November events. These extremely suppressed days, while less numerous than in the previous months, nevertheless provided a further opportunity to examine the boundary layer convective cloud patterns during the early part of suppressed periods.

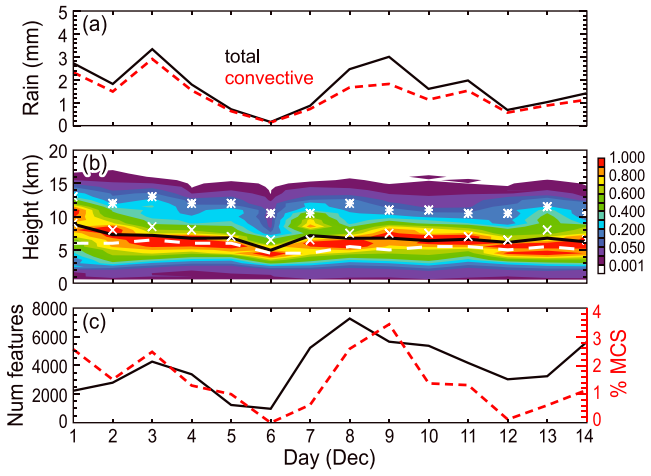

Figure 14. (a–c) Same as in Figure 2 except for the 1–14 December time period.

Figure 15a reveals nonprecipitating clouds organized into lines in the eastern half of the radar domain on 7 December 2011 at 1031 UTC. At this time, these lines, particularly to the east and southeast of the radar, were aligned parallel to the low-level flow (Figure 15b) and wind shear (Figure 4g). An RHI through a line located to the east-northeast at this time (Figure 16) offers another increasingly familiar sight. Among layers of moisture gradients, characterized by reflectivity less than

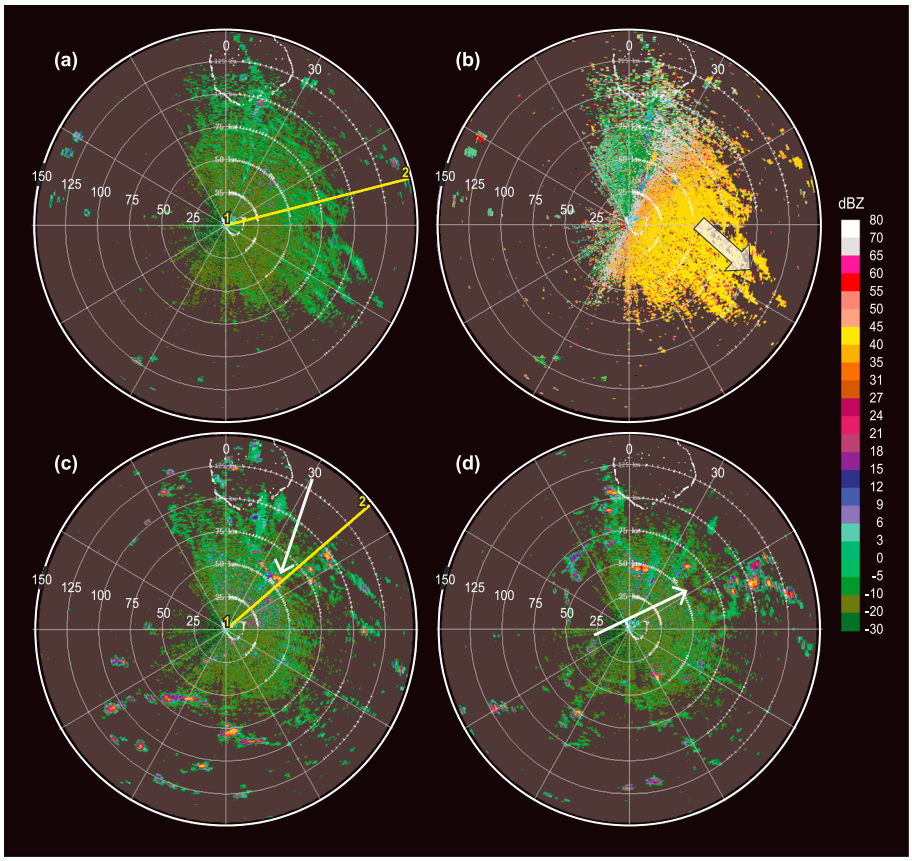

Figure 15. Same as in the reflectivity surveillance figures for October and November (e.g., Figure 3) except for 7 December 2014 showing (a) reflectivity at 1101 UTC, (b) radial velocity at 1101 UTC, (c) reflectivity at 1416 UTC, and (d) reflectivity at 1546 UTC. The yellow lines in Figures 15a and 15c indicate the location of the RHIs in Figure 15 and Figures 16a and 16b, respectively. The white arrow in Figure 15c indicates the cell featured in the RHI and in Figure 15d the echo-free area corresponding to a cold pool. The block arrow in Figure 15b indicates the direction of the 0–1.5 km wind shear vector at 1200 UTC.

−15 dBZ, near-zero Z and Z_{DR} can be seen around 1 km, corresponding, yet again, to L_{DR} values around −25 dB, ρ_{HV} near 1, and PID-identified cloud droplets. Also of note in this RHI is the radial velocity cross section, reflecting the stronger, deeper westerlies characteristic of this month. Despite this difference in the environmental wind profile of December from previous months, the boundary layer organization of clouds into lines initially parallel to the low-level shear continued to emerge as a repeatable observation during the early days of suppressed periods. Also similar to the previous months, precipitating features later developed along these boundary layer rolls with their cold pools dominating the cloud pattern later in the day.

For example, convective features were observed on this day (Figure 15c), after they formed in the northeast sector later in the afternoon along the lines oriented parallel to the shear. An RHI through one of these features (Figures 17a and 17b) highlights shallow but heavily precipitating convection similar to that seen during the early stages of the October and November suppressed periods. Echo tops barely exceeded the melting level in this example, consistent with the 50th percentile of maximum echo-top heights for features on this day, although deeper features were occasionally observed on this and most other days of the suppressed period, with less variation in echo-top statistics throughout this period compared to October and November (Figures 2, 9, and 14). Reflectivity exceeded 50 dBZ in the convective feature seen in Figure 17a, and the PID indicated heavy rain near the surface (Figure 17b), suggesting an efficient warm-rain process (i.e., drop coalescence growth at low levels). While precipitating features such as this one left behind cold pools (Figure 15d), subsequent development of raining clouds at the edges of cold pools was limited on this day as it was during the early suppressed days of October and November. As a result, the overall rain rates were again lower than those that occurred later in the suppressed period (Figure 14). In addition, the rolls along which the convective features formed were no longer evident at this later time of day (~1500 UTC),

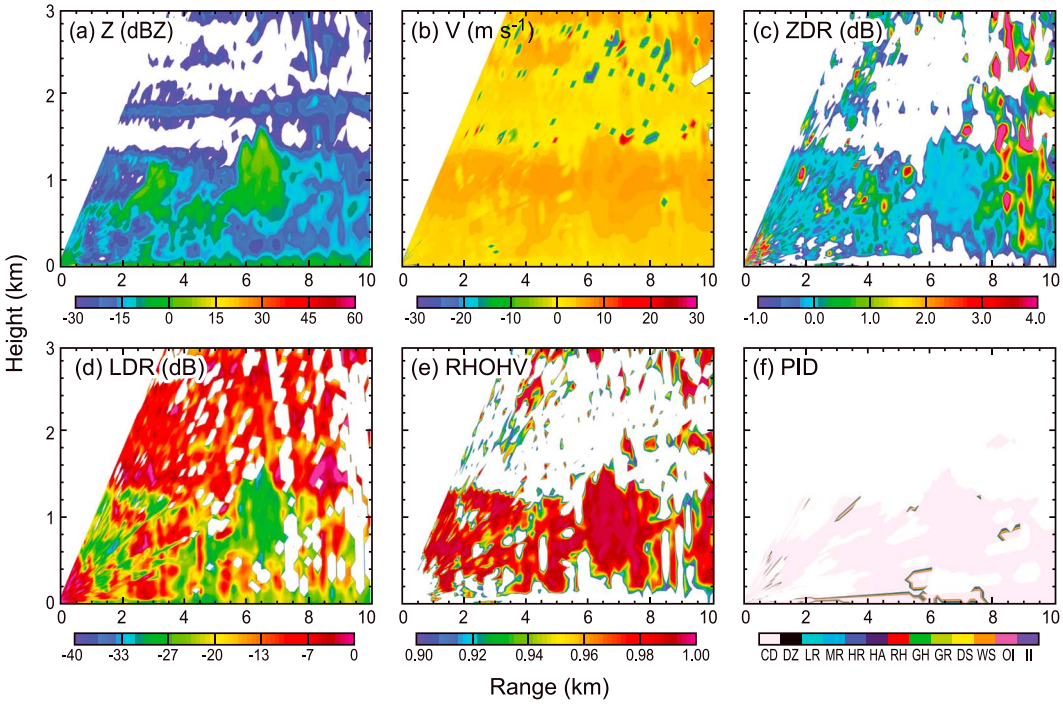

Figure 16. (a–f) Same as in Figure 1 except for 1105 UTC on 7 December 2011 at an azimuth of 76°.

possibly owing to the reduction in wind shear (Figure 4h). *Ferrare et al*. [1991] noted that such linear features become less elongated throughout the day because of a decrease in boundary layer wind speed (and hence shear) and an increase in thermal instability. This tendency for rolls to be less organized as the boundary layer becomes more buoyantly unstable was also noted in *Weckwerth et al*. [1999], who, furthermore, described an evolution from rolls toward unorganized "random" convection when wind speeds were $>3\,\mathrm{m\,s^{-1}}$ in the boundary layer, which was observed for this December case in Figure 17.

These 2–3 days with boundary layer lines and shallow, precipitating features were the only days in December with radar characteristics similar to those of the early suppressed periods of October and November. As was shown in the time series (Figure 14), rainfall, number of features, and percentage of MCSs increased rapidly as 8 December approached, with generally deep convection occurring through the remainder of the month. This precipitating deeper convection was nonetheless generally shallower than the deepest convection observed toward the ends of the October and November suppressed periods. This result is consistent with observations of shallower convection during December described in *Rowe and Houze* [2014].

Whereas an increasing dominance of cold pool interactions occurred over roughly a week during October and November, the echo pattern of December transitioned from suppressed to large mesoscale systems spanning the entire radar domain over the course of only a few days. An example from 0901 UTC on 8 December 2011 shows a squall line oriented from the north-northwest to the south-southeast (Figure 18a), with increased stratiform precipitation in contrast to the smaller precipitating features in the earlier suppressed periods of all 3 months in this study. The corresponding radial velocity PPI (Figure 18b) highlights the strong westerly winds unique to this time period that led to these traveling linear squall lines, reminiscent of certain MCSs occurring over other tropical oceanic regions [*Zipser*, 1969; *Houze and Betts*, 1981; *LeMone et al*., 1998; *Houze et al*., 2000; *Mechem et al*., 2002, and others]. As this squall line propagated across the domain, a line of convection oriented perpendicular to the larger squall line was observed (Figure 18c). While the squall line weakened as it entered into the RHI sectors, an RHI through the perpendicular convective line (Figures 17c and 17d) reveals a larger precipitation feature reminiscent of the larger features with increasing stratiform components observed later in October and November. Despite the rapid upscale growth of the cloud systems, there was no graupel identified in the PID in this RHI example or in earlier RHIs when this precipitating feature was slightly deeper (not shown). While PID-inferred graupel was observed in some of these December MCSs, statistics showed that it was limited in vertical extent, along with

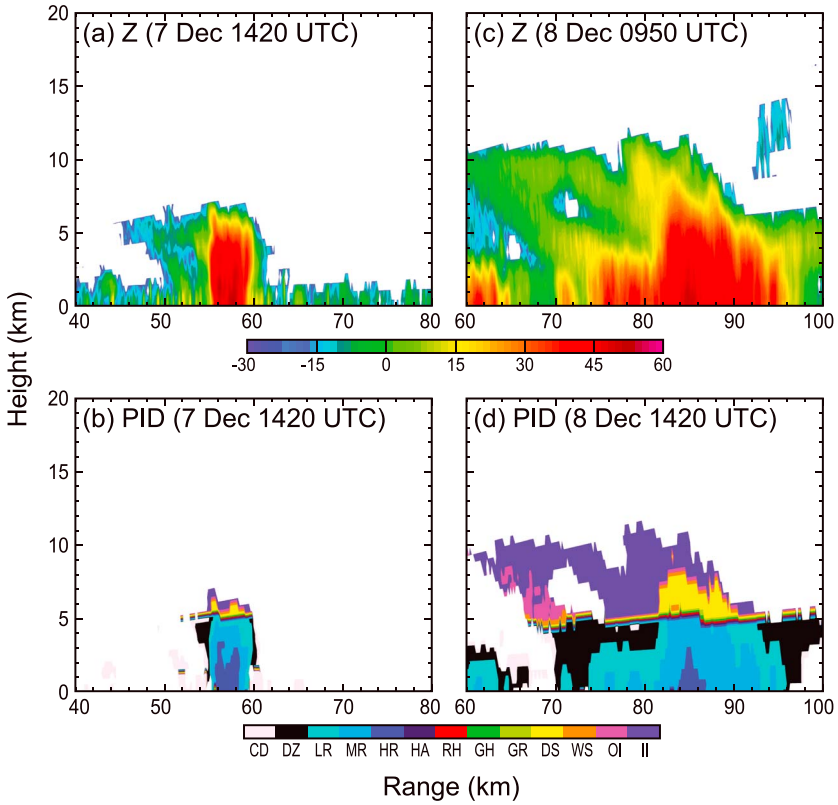

Figure 17. RHIs of convection at (a and b) 1420 UTC on 7 December at 50° azimuth and at (c and d) 0950 UTC on 8 December at 116° azimuth. Figures 17a and 17c show reflectivity, and Figures 17b and 17d show particle identification, with categories defined as in Figure 1.

overall shallower echo tops than those of MCSs observed in October and November [*Rowe and Houze*, 2014]. This pattern of shallower but fast-moving squall lines began on this day and continued to be observed through the most active phase of December. It is speculated that the limited vertical extent and tendency toward squall line formation was related to the stronger shear in December compared to October and November.

4. The Diurnal Cycle of Convection

Examples in the previous section described a pattern wherein nonprecipitating clouds organized along lines (or, occasionally, open-cell patterns) provided a focal point for precipitating convection to form during suppressed periods leading up to active MJO periods. This low-altitude cloud organizational process is critical to understanding how the precipitating cloud population of an active MJO forms. The examples shown in the previous section exhibited a diurnal rhythm, which will be described fully in this section. Because the October and November cases were clear manifestations of MJO behavior (while the large-scale interpretation of the December event was less clear and somewhat controversial as to its representativeness of MJO conditions), this section focuses on the diurnal cycle as it occurred during October and November.

All grid points within precipitating features (i.e., all grid points meeting the 15 dBZ threshold, regardless of feature type or life cycle stage) are presented as daily frequencies of occurrence as a function of local time of day (LT = UTC + 5 h) for October (Figure 19a) and November (Figure 19c). These frequencies were normalized by dividing the number of points containing precipitating echo at a given time by the maximum number of such points at the time of day when the most were present. This normalized quantity's diurnal variation may be interpreted as the variation of the probability of occurrence of a grid point containing rain as a function of time of day for each day during the suppressed periods considered here. Color-filled contours in Figures 19b and 19d indicate the total count of individual precipitating features present in the radar domain

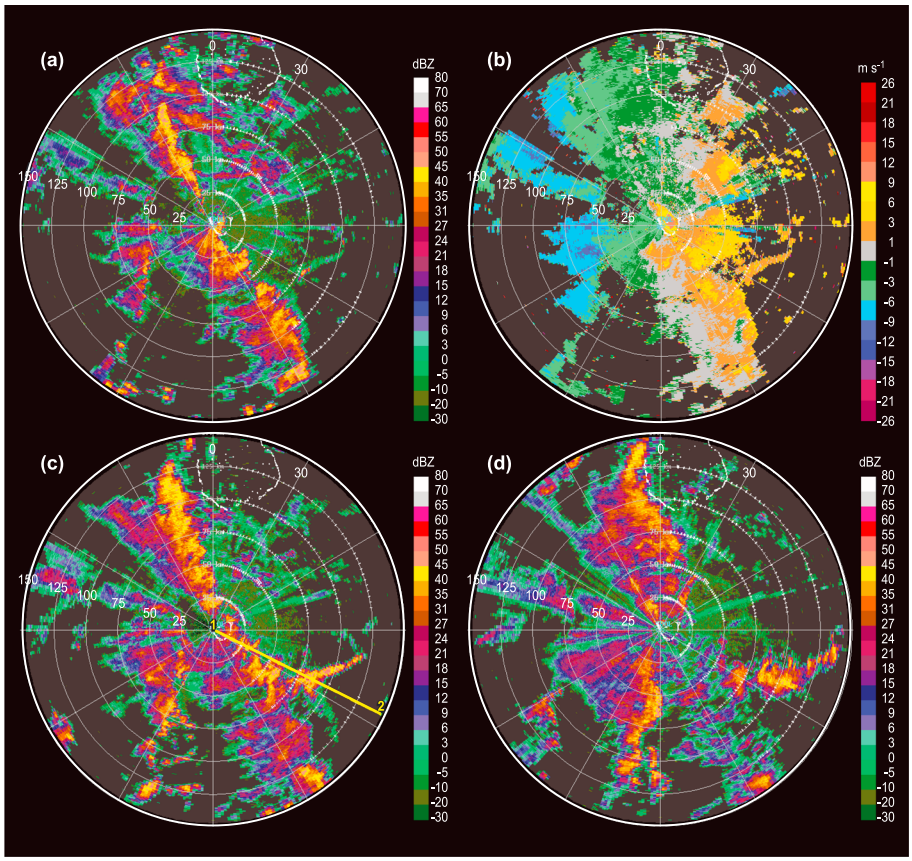

Figure 18. Same as in Figure 3 except for 8 December 2011 showing (a) reflectivity at 0901 UTC, (b) radial velocity at 0901 UTC, (c) reflectivity at 0946 UTC, and (d) reflectivity at 1046 UTC. The yellow line in Figure 18c indicates the location of the RHI in Figures 16c and 16d.

at each hour and day during the October and November suppressed periods, respectively. The benefit of using these two types of metrics for this analysis is to include both the large number of individual, but relatively small sub-MCS features, which dominated the suppressed periods, while also being able to understand when the largest, but less frequent, precipitating features occurred. Based on the time series and examples presented in section 3, early suppressed periods in this discussion refer (coincidentally) to dates 5–7 for each month, middle to dates 8–11, and later to dates 12–14.

Recall from the time series in Figures 2 and 9 that the total number of features tended to be lowest for the respective months during the early days of the suppressed periods. Figures 19b and 19d reflect this minimal occurrence in the generally lower number of features observed in the early dates regardless of time of day. In addition to an increase in total number of features throughout the suppressed period, the number of precipitating features exhibited a relative minimum in feature occurrence around 09:00–11:00 LT in October (Figure 19b) and 07:00–09:00 LT in November (Figure 19d), with the exception of 12 November. This pattern likely indicated the time of initiation of precipitating convective elements along the boundary layer lines and open cells that dominated the scene during the late morning, as illustrated by the previous section's examples. *Ruppert and Johnson* [2015] described a related morning peak in low-level echo-top frequency, where low-level echo tops peaked around 11:00 and 09:00 LT during the October and November suppressed periods, respectively, while echo area coverage was increasing. They related this trend of increasing echo/features during the morning to the diurnal cycle in air temperature; their suggestion is that the boundary layer was warmed and destabilized by increasing SST, leading to an afternoon peak in cumulus clouds. The examples in section 3 showed precipitating features producing cold pools that led to secondary initiation of convection, especially precipitating convection, after local noon. Further implicating the role of cold pools in this feedback cycle, *Ruppert and Johnson* [2015] described a drop in air temperature owing to the passage of cold pools around 14:00 LT during these suppressed periods.

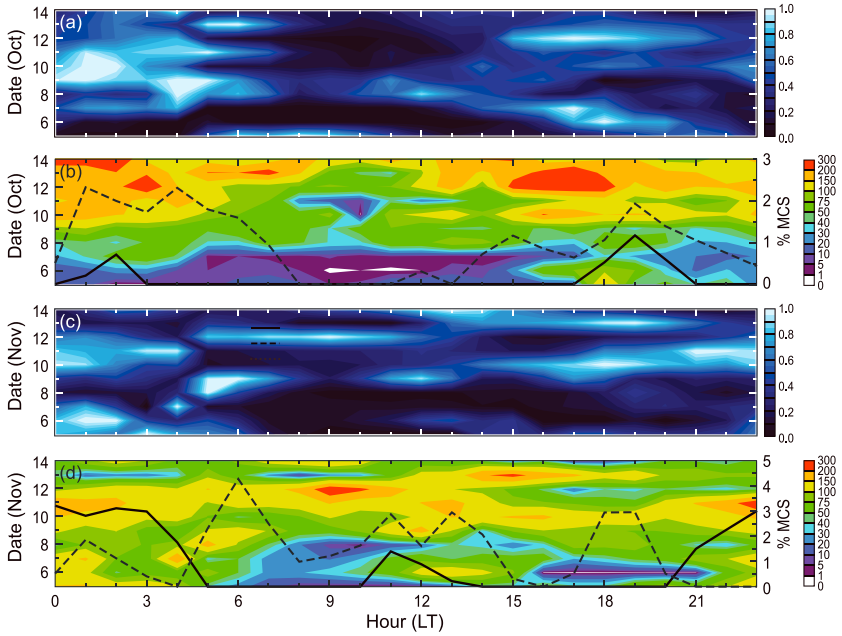

Figure 19. (a and c) Color-filled contours show the frequency of occurrence of all precipitating feature grid points identified for each day of the October and November suppressed periods, respectively, as a function of local time. Frequencies are presented as a fraction from 0 to 1, with 1 corresponding to the number present at the time of maximum occurrence of precipitating grid points for the given day. (b and d) Color-filled contours show total number of precipitating features for each hour and day in the October and November suppressed periods, respectively. Overlaid black curves show the time series of the relative percentage of precipitating features meeting MCS criteria (100 km major axis) for middle (8–11, solid) and later (12–14, dashed) sections of each monthly suppressed period.

This chain reaction is reflected in Figure 19 whereby localized maxima in feature occurrence were generally observed in the afternoon throughout the suppressed periods. There were, however, additional maxima that were observed during other times of the day, particularly overnight during the latter half of the suppressed periods. For the middle and later stages of the suppressed periods in DYNAMO, when more numerous and deeper convective features were observed compared to the earliest days of the suppressed periods (Figures 2 and 9), relatively high frequencies of precipitating features often persisted after midnight. For example, while the most probable time for grid points associated with precipitating features to occur on 6 October was around 18:00 LT, by 10 October, the most probable time was around 01:00 LT (Figure 19a), and numerous precipitating features were also observed in the early morning hours on the later suppressed days of October (Figure 19b). Such behavior is consistent with the findings of *Chen and Houze* [1997], who found a bimodal distribution of starting times of small mesoscale systems ($<$80 km in dimension) identified in infrared imagery over the tropical western Pacific; some starting late afternoon in sync with the solar heating and some starting in the predawn hours, likely triggered by the outflows of other convection. Indeed, the predawn peak did not occur in the most convectively suppressed period of the October MJO. The 11 November case exhibited similar behavior, with a maximum of precipitating echo occurring after 2100 UTC (Figure 19b), with precipitating features continually observed even after sunrise during the later suppressed days of this month (Figure 19d).

In the examples presented in section 3 from the middle and later stages of the suppressed periods, it was shown that convection began to cluster and grow upscale into mesoscale features (small MCSs) near intersections of cold pool boundaries later in the afternoon. To further investigate a possible diurnal trend in mesoscale organization, time series of relative percentages of precipitating features meeting MCS criteria, calculated for every hour, are overlaid in Figures 19b and 19d. Only the middle (solid) and later (dashed) dates are included in these MCS time series (Figures 19b and 19d) as no precipitation features exceeded the 100 km major axis threshold during the early dates of the suppressed periods, consistent with the lack of clustering of convection shown in early suppressed examples from section 3. The precipitating features that tended to occur most frequently during the afternoon of the early-suppressed periods were associated solely with

sub-MCS features. They were small, few, and widely separated and thus not likely to generate cold pools in sufficient number and strength to spawn secondary stronger precipitating convection.

During the middle and later stages of the October suppressed period, a small percentage of precipitation features reached MCS scale, particularly during the later stages, with maxima during the afternoon and evening then again during the overnight hours (Figure 19b). The late afternoon peak in frequency of precipitating features preceded the evening peak in MCS occurrence. This behavior indicates that numerous sub-MCS-scale features initially contributed strongly to the precipitation coverage throughout the afternoon while MCSs increasingly contributed to the number of features (Figure 19b) and overall frequency of occurrence of precipitating grid points (Figure 19a) as the evening progressed. This sequence is consistent with the upscale growth observed during the evening of the later suppressed dates during October in the examples shown in section 3 and with the general fact that MCS features of larger size have longer lifetimes, which strongly influence their diurnal effects [*Chen and Houze*, 1997]. The relatively few MCSs that peaked in occurrence at 19:00 LT moved out of the radar domain resulting in a decrease in MCS percentages by local midnight. These few MCSs, however, left behind outflow boundaries that contribute to the formation of additional precipitating features, which subsequently clustered and grew upscale to produce another overnight peak in MCS occurrence before dissipating by sunrise.

The trend of increasing upscale growth overnight was also observed during the middle stages of the November suppressed period, as clustering of precipitating features occurred along cold pools formed from afternoon convection. During the later stages, however, MCS occurrence also peaked midday. This trend is dominated by a combination of MCSs that continuously formed along outflow boundaries overnight on 12 November, left behind by previous MCSs that had moved out of the domain on 11 November, and a series of MCSs that moved into the domain throughout the morning on 12 November, with additional formation and upscale growth of precipitation features along outflow boundaries advancing ahead of the system. Despite this different pattern on 12 November, overall there was an observed trend of upscale growth of convection throughout the evening toward a few MCSs during the latter portions of the suppressed periods in October and November. This life cycle behavior with MCSs continuing into the early morning hours is consistent with life cycles found by *Chen and Houze* [1997] and with the nocturnal peak in rainfall described in other tropical oceanic studies [e.g., *Albright et al*., 1981; *Janowiak et al*., 1994; *Sui et al*., 1997; *Johnson et al*., 2001; *Kikuchi and Wang*, 2008; *Bellenger et al*., 2010; *Ruppert and Johnson*, 2015]. This trend characterized the transition toward the active MJO periods of DYNAMO, which were characterized by more numerous and larger MCSs that also persisted into the early morning hours [e.g., *Powell and Houze*, 2013, 2015; *Barnes and Houze*, 2014; *Rowe and Houze*, 2014; *Xu and Rutledge*, 2014].

5. Conclusions and Broader Implications

It is well known that cold pools produced by precipitating convective clouds can spread out and trigger secondary convection [e.g., *Karan and Knupp*, 2009; *Snodgrass et al*., 2009; *Li et al*., 2014; *Schlemmer and Hohenegger*, 2014; *Feng et al*., 2015]. However, cold pool triggering only occurs after precipitating convection has developed. Therefore, to completely understand the initiation of the active precipitating phase of an MJO, an understanding of the behavior of the nonprecipitating clouds leading up to the first precipitating features is required. In this study, the S-PolKa radar data from DYNAMO/AMIE were used to investigate the nonprecipitating convective cloud behavior that preceded the first precipitating convective elements leading up to the occurrence of precipitating convective clouds, which produced cold pools and secondary precipitating convection. While previous studies using the S-PolKa observations have described the precipitating clouds, this study took advantage of the high sensitivity of this radar to detect and analyze the behavior of the nonprecipitating clouds as they organized and evolved into a population containing precipitating elements. The dual-polarimetric capability of S-PolKa allowed the nonprecipitating clouds to be distinguished from clear-air Bragg scatter echoes produced by humidity gradients, thereby providing a means to trace echoes associated with nonprecipitating clouds. The Bragg scatter return combined with the nonprecipitating cloud echoes further allowed the boundaries of cold pools produced by rain showers to be identified and tracked. This approach is similar to previous field campaigns using S-band radar to investigate cloud initiation and structure under synoptically suppressed conditions [e.g., *Lima and Wilson*, 2008; *Zuidema et al*., 2012]. The three-dimensional scanning by S-PolKa made it possible to map the horizontal patterns of

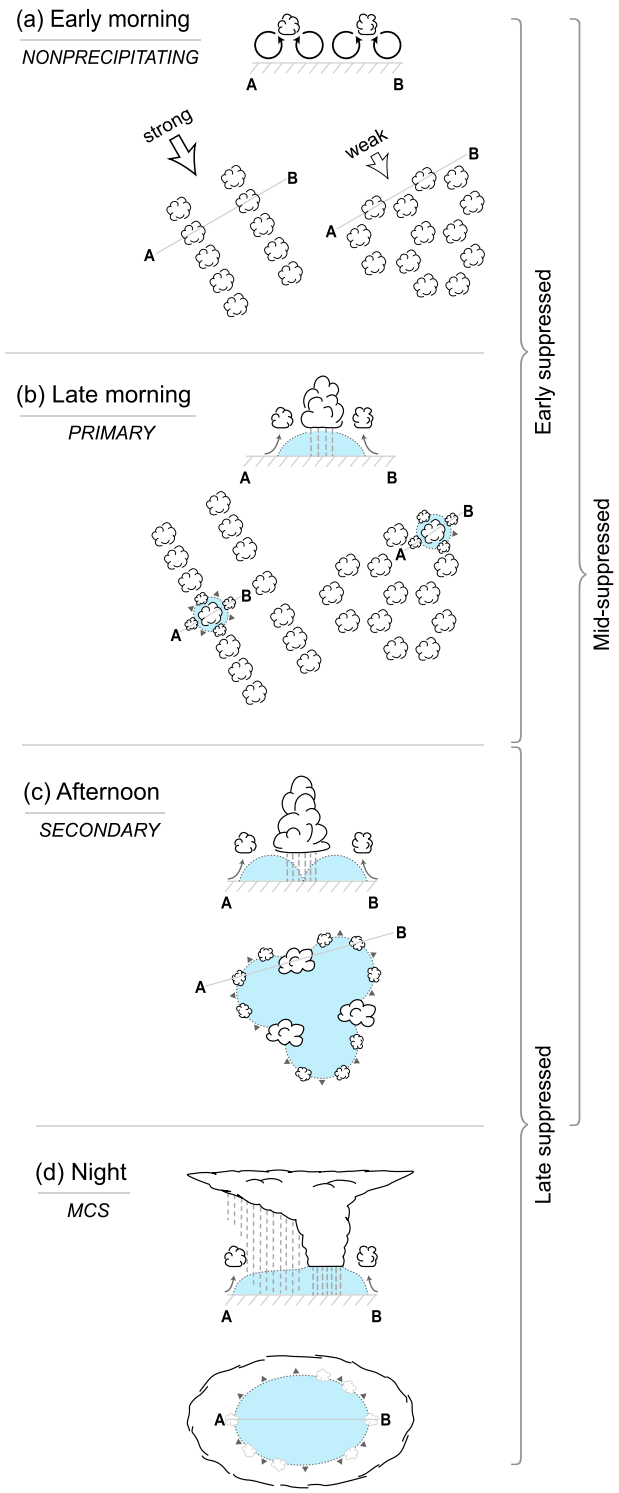

Figure 20. A schematic showing (a) the organization of nonprecipitating clouds, (b) the production of cold pools from precipitating cells, (c) the secondary initiation of deeper convection along intersecting cold pool boundaries, and (d) the eventual upscale growth to MCSs overnight during the later suppressed periods. Note that these drawings are not to scale. The cold pool in Figure 20d is much bigger than the cold area in Figure 20c. Early, middle, and late suppressed brackets refer to the general time within the suppressed periods when these sequences of events are observed. Local times of day when these processes occur are indicated at the top.

nonprecipitating clouds. This spatial organization of the nonprecipitating cloud patterns was examined in relation to the low-level wind and wind shear prevailing over the central Indian Ocean. Those nonprecipitating clouds that began to precipitate were identified, as were their associated cold pools. The precipitating clouds and cold pools were both tracked in time. From this analysis of the S-PolKa reflectivity patterns, the evolution of the convective population from these suppressed periods into more active MJO convective periods has been described.

The evolution of the cloud population from suppressed to active periods that is inferred from the S-PolKa observations is synthesized in Figure 20. After sunrise, in relatively moderate to strong low-level wind conditions, nonprecipitating clouds occurred in lines in the boundary layer (Figure 20a) that were initially oriented nearly parallel to the low-level wind shear direction. Boundary layer overturning in rolls (and/or open cells) produce lines of concentrated low-level moisture convergence and upward air motions that can connect the boundary layer moisture maxima with the free atmosphere [e.g., *Weckwerth et al*., 1996], and the observed nonprecipitating cloud lines fit this interpretation. Under weaker wind conditions, such as during early November, the organization of the field of nonprecipitating convective clouds foreshadowing MJO initiation tended toward an open-cell pattern.

Later in the morning (Figure 20b), the first precipitating clouds formed on these lines of nonprecipitating convective clouds. There were instances when the intersections between younger and older lines may have promoted formation of precipitating convective features. These generally shallow clouds that produced brief rain showers along the boundary layer lines/open cells often produced small cold pools, at whose boundary secondary (relative to the initial convection that produced the cold pool) clouds were triggered, thus starting a chain reaction.

During the early part of the suppressed periods, secondary convection triggered at cold pool boundaries remained relatively shallow, dominated by warm-rain processes, with most dissipating by evening. However, during the middle stages of the suppressed periods, when midlevel moistening had increased, deeper, more numerous features occurred, associated with increased clustering of convection along intersecting cold pool boundaries throughout the afternoon (Figure 20c). The secondary precipitating convective features produced their own cold pools, leading to additional initiation of precipitating convection and clustering, with some long-lived precipitating features growing to MCS scale in the overnight hours. By the end of the suppressed periods, upscale growth led, at times, to deep and broad MCSs with increased stratiform contribution to rainfall that persisted into morning (Figure 20d). These MCSs produced their own (much broader) cold pools, which could lead to further convective initiation in the morning, differing from the precipitating features that initiated in the morning along boundary layer cloud streets or open cells during the early suppressed periods.

Despite the similarities in the trends, subtle differences were apparent among the three suppressed periods examined. October was characterized by gradual moistening and an extended time period dominated by the boundary layer rolls. November, with its more rapid moistening at low and middle levels, initially exhibited similar rolls, but wind speeds were weaker, and the dominant mode of initial cloud organization was in the form of open cells rather than long linear cloud streets. December differed in that the large-scale dynamical evolution was atypical of MJO development; December was uniquely characterized by stronger, deeper westerly winds. Despite a relatively shorter period of shallow, isolated cumulus clouds, the nonprecipitating clouds in December often organized into lines during these early suppressed days, similar to those of the October and November suppressed periods preceding more prototypical MJO onset. Although fast-moving squall lines quickly became the norm in mid-December, continuing to be observed throughout the rest of the month, the diurnal cycle and evolving pattern of the boundary layer, particularly the trends throughout the transition from suppressed to active periods, appeared to be consistent across multiple instrument platforms (including the soundings and satellite data described in *Ruppert and Johnson* [2015]).

The conclusions embodied in the schematic in Figure 20 emphasize the need for accurate representation of the oceanic boundary layer in models aimed at predicting MJO onset. While representation of cold pools from rain showers is also important in such models [e.g., *Feng et al*., 2015], the cold pools that disturb the boundary layer are a product of the precipitating convection, which is preceded by organization of the nonprecipitating convective cloud field. In this study, it became apparent that such organization can occur

in the form of boundary layer rolls or open cellular overturning. The formation of the first clouds capable of precipitating during early DYNAMO suppressed periods took place in the context of these organizational patterns of the shallow nonprecipitating cloud field. Predicting the boundary layer phenomena involved in organizing the low-level nonprecipitating cloud field is therefore crucial to predicting the cumulus clouds that are robust enough to precipitate and generate cold pools and set off the chain reaction that assists the evolution of the cloud population toward a more active MJO state.

Acknowledgments

This research is supported by Department of Energy Atmospheric Sciences Research grant DE-SC0008452 and National Science Foundation grants AGS-1355567 and AGS-1059611. We appreciate the efforts of the NCAR S-PolKa team in the collection and quality control of the S-PolKa radar data and Stacy Brodzik for managing the radar data archive and software used in this study. S-PolKa radar data and details regarding the quality control are available at http://www.eol.ucar.edu/projects/dynamo/spol/. Elizabeth Thompson and two anonymous reviewers provided insightful comments. We especially thank Beth Tully for her work with the graphics and editing.

References

Albright, M. D., D. R. Mock, E. E. Recker, and R. J. Reed (1981), A diagnostic study of the diurnal rainfall variation in the GATE B-scale area, *J. Atmos. Sci.*, *38*, 1429–1445.

Asai, T. (1970a), Stability of a plane parallel flow with variable vertical shear and unstable stratification, *J. Meteorol. Soc. Jpn.*, *48*, 129–139.

Asai, T. (1970b), Three-dimensional features of thermal convection in a plane Couette flow, *J. Meteorol. Soc. Jpn.*, *48*, 18–29.

Asai, T. (1972), Thermal instability of a shear flow turning the direction with height, *J. Meteorol. Soc. Jpn.*, *50*, 525–532.

Barnes, G. M., and K. Sieckman (1984), The environment of fast- and slow-moving tropical mesoscale convective cloud lines, *Mon. Weather Rev.*, *112*, 1782–1794.

Barnes, H. C., and R. A. Houze (2014), Precipitation hydrometeor type relative to the mesoscale airflow in oceanic deep convection of the Madden-Julian Oscillation, *J. Geophys. Res. Atmos.*, *119*, 13,990–14,014, doi:10.1002/2014JD022241.

Bellenger, H., Y. N. Takayabu, T. Ushiyama, and K. Yoneyama (2010), Role of diurnal warm layers in the diurnal cycle of convection over the Indian Ocean during MISMO, *Mon. Weather Rev.*, *138*, 2426–2433.

Benedict, J. J., and D. A. Randall (2007), Observed characteristics of the MJO relative to maximum rainfall, *J. Atmos. Sci.*, *64*, 2332–2354.

Cetrone, J., and R. A. Houze Jr. (2006), Characteristics of tropical convection over the ocean near Kwajalein, *Mon. Weather Rev.*, *134*, 834–853.

Chen, S. S., and R. A. Houze Jr. (1997), Diurnal variation and life cycle of deep convective systems over the tropical Pacific warm pool, *Q. J. R. Meteorol. Soc.*, *123*, 357–388.

Davison, J. L. (2014), Investigation of the island effect on mixed layer top and transition layer top elevations using Bragg scattering layer (BSL) analysis of clear-air S-Pol radar retrievals at the Gan site during CINDY2011/DYNAMO/AMIE, paper presented at 31st Conference on Hurricanes and Tropical Meteorology, Am. Meteorol. Soc., San Diego, Calif.

Davison, J. L., R. M. Rauber, and L. Di Girolamo (2013), A revised conceptual model of the tropical marine boundary layer. Part II: Detecting relative humidity layers using Bragg scattering from S-band radar, *J. Atmos. Sci.*, *70*, 3025–3046.

Del Genio, A. D., Y. Chen, D. Kim, and M.-S. Yao (2012), The MJO transition from shallow to deep convection in CloudSat/CALIPSO data and GISS GCM simulations, *J. Clim.*, *25*, 3755–3770.

Feng, Z., S. A. McFarlane, C. Schumacher, S. Ellis, J. Comstock, and N. Bharadwaj (2014), Constructing a merged cloud-precipitation radar dataset for tropical convective clouds during the DYNAMO/AMIE experiment at Addu Atoll, *J. Atmos. Oceanic Technol.*, *31*, 1021–1042.

Feng, Z., S. Hagos, A. K. Rowe, C. D. Burleyson, M. N. Martini, and S. P. de Szoeke (2015), Mechanisms of convective cloud organization of cold pools over tropical warm ocean during the AMIE/DYNAMO field campaign, *J. Adv. Model. Earth Syst.*, *07*, 357–381, doi:10.1002/2014MS000384.

Ferrare, R. A., J. L. Schols, E. W. Eloranta, and R. Coulter (1991), Lidar observations of banded convection during BLX83, *J. Appl. Meteorol.*, *30*, 312–326.

Gottschalck, J., P. E. Roundy, C. J. Schreck III, A. Vintzileos, and C. Zhang (2013), Large-scale atmospheric and oceanic conditions during the 2011-12 DYNAMO field campaign, *Mon. Weather Rev.*, *105*, 1171–1188.

Hannah, W. M., and E. D. Maloney (2011), The role of moisture-convection feedbacks in simulation the Madden-Julian Oscillation, *J. Clim.*, *24*, 2754–2770.

Houze, R. A., Jr., and A. K. Betts (1981), Convection in GATE, *Rev. Geophys. Space Phys.*, *19*, 541–576.

Houze, R. A., Jr., S. S. Chen, D. E. Kingsmill, Y. Serra, and S. E. Yuter (2000), Convection over the Pacific warm pool in relation to the atmospheric Kelvin-Rossby wave, *J. Atmos. Sci.*, *57*, 3058–3089.

Janowiak, J. E., P. A. Arkin, and M. Morrissey (1994), An examination of the diurnal cycle in oceanic tropical rainfall using satellite and in situ data, *Mon. Weather Rev.*, *122*, 2296–2311.

Johnson, R. H., and P. E. Ciesielski (2013), Structure and properties of Madden-Julian Oscillations deduced from DYNAMO sounding arrays, *J. Atmos. Sci.*, *70*, 3157–3179.

Johnson, R. H., P. E. Ciesielski, and J. A. Cotturone (2001), Multiscale variability of the atmospheric mixed layer over the western Pacific warm pool, *J. Atmos. Sci.*, *58*, 2729–2750.

Johnson, R. H., P. E. Ciesielski, J. H. Ruppert Jr., and M. Katsumata (2015), Sounding-based thermodynamic budgets for DYNAMO, *J. Atmos. Sci.*, *72*, 598–622.

Karan, H., and K. Knupp (2009), Radar and profiler analysis of colliding boundaries: A case study, *Mon. Weather Rev.*, *137*, 2203–2222.

Kikuchi, K., and B. Wang (2008), Diurnal precipitation regimes in the global tropics, *J. Clim.*, *21*, 2680–2696.

Knight, C. A., and L. J. Miller (1998), Early radar echoes from small, warm cumulus: Bragg and hydrometeor scattering, *J. Atmos. Sci.*, *55*, 2974–2992.

Knight, C. A., J. Vivekanandan, and S. G. Lasher-Trapp (2002), First radar echoes and the early ZDR history of Florida cumulus, *J. Atmos. Sci.*, *59*, 1454–1472.

Knight, C. A., L. J. Miller, and R. A. Rilling (2008), Aspects of precipitation development in trade wind cumulus revealed by differential reflectivity at S band, *J. Atmos. Sci.*, *65*, 2563–2580.

Kuettner, J. P. (1959), The band structure of the atmosphere, *Tellus*, *2*, 267–294.

Kuettner, J. P. (1971), Cloud bands in the Earth's atmosphere, *Tellus*, *23*, 404–425.

Kumar, V. V., A. Protat, C. Jakob, and P. T. May (2014), On the atmospheric regulation of the growth of moderate to deep cumulonimbus in a tropical environment, *J. Atmos. Sci.*, *71*, 1105–1120.

Kuo, H. L. (1963), Perturbations of plane Couette flow in stratified fluid and origin of cloud streets, *Phys. Fluids*, *6*, 195–211.

LeMone, M. A., E. J. Zipser, and S. B. Trier (1998), The role of environmental shear and thermodynamic conditions in determining the structure and evolution of mesoscale convective systems during TOGA COARE, *J. Atmos. Sci.*, *55*, 3493–3518.

Li, Z., P. Zuidema, and P. Zhu (2014), Simulated convective invigoration processes at trade wind cumulus cold pool boundaries, *J. Atmos. Sci.*, *71*, 2823–2841.

Lima, M. A., and J. W. Wilson (2008), Convective storm initiation in a moist tropical environment, *Mon. Weather Rev.*, *136*, 1847–1864.

Madden, R. A., and P. R. Julian (1971), Detection of a 40-50 day oscillation in the zonal wind in the tropical Pacific, *J. Atmos. Sci.*, *28*, 702–708.
Madden, R. A., and P. R. Julian (1972), Description of global-scale circulation cells in the tropics with a 40-50 day period, *J. Atmos. Sci.*, *29*, 1109–1123.
Mechem, D. B., R. A. Houze Jr., and S. S. Chen (2002), Layer inflow into precipitating convection over the western tropical Pacific, *Q. J. R. Meteorol. Soc.*, *128*, 1997–2030.
Melnikov, V. M., R. J. Doviak, D. S. Zrnić, and D. J. Stensrud (2011), Mapping Bragg scatter with a polarimetric WSR-88D, *J. Atmos. Oceanic Technol.*, *28*, 1273–1285.
Minor, H. A., R. M. Rauber, S. Göke, and L. Di Girolamo (2011), Trade wind cloud evolution observed by polarization radar: Relationship to giant condensation nuclei concentrations and cloud organization, *J. Atmos. Sci.*, *68*, 1075–1096.
Mohr, C. G., and R. L. Vaughan (1979), An economical procedure for Cartesian interpolation and display of reflectivity factor data in three-dimensional space, *J. Appl. Meteorol.*, *18*, 661–670.
Nesbitt, S. W., R. Cifelli, and S. A. Rutledge (2006), Storm morphology and rainfall characteristics of TRMM precipitation features, *Mon. Weather Rev.*, *134*, 2702–2721.
Nuss, W. A., and D. W. Titley (1994), Use of multiquadric interpolation for meteorological objective analysis, *Mon. Weather Rev.*, *122*, 1611–1631.
Powell, S. W., and R. A. Houze Jr. (2013), The cloud population and onset of the Madden-Julian Oscillation over the Indian Ocean during DYNAMO-AMIE, *J. Geophys. Res. Atmos.*, *118*, 11,979–11,995, doi:10.1002/2013JD020421.
Powell, S. W., and R. A. Houze Jr. (2015), Effect of dry large-scale vertical motions on initial MJO convective onset, *J. Geophys. Res. Atmos.*, *120*, 4783–4805, doi:10.1001/2014JD022961.
Riley, E. M., B. E. Mapes, and S. N. Tulich (2011), Clouds associated with the Madden-Julian Oscillation: A new perspective from CloudSat, *J. Atmos. Sci.*, *68*, 3032–3051.
Rowe, A. K., and R. A. Houze Jr. (2014), Microphysical characteristics of MJO convection over the Indian Ocean during DYNAMO, *J. Geophys. Res. Atmos.*, *119*, 2543–2554, doi:10.1002/2013JO020799.
Ruppert, J. H., Jr., and R. H. Johnson (2015), Diurnally modulated cumulus moistening in the preonset stage of the Madden-Julian Oscillation during DYNAMO, *J. Atmos. Sci.*, *72*, 1622–1647.
Schlemmer, L., and C. Hohenegger (2014), The formation of wider and deeper clouds as a result of cold-pool dynamics, *J. Atmos. Sci.*, *71*, 2842–2858.
Snodgrass, E. R., L. Di Girolamo, and R. M. Rauber (2009), Precipitation characteristics of trade wind clouds during RICO derived from radar, satellite, and aircraft measurements, *J. Appl. Meteorol. Climatol.*, *48*, 464–483.
Steiner, M., R. A. Houze Jr., and S. E. Yuter (1995), Climatological characterization of three-dimensional storm structure from operational radar and rain gauge data, *J. Appl. Meteorol.*, *34*, 1978–2007.
Straka, J. M., D. S. Zrnić, and A. V. Ryzhkov (2000), Bulk hydrometeor classification and quantification using polarimetric radar data: Synthesis of relations, *J. Appl. Meteorol.*, *39*, 1341–1372.
Sui, C.-H., K.-M. Lau, Y. N. Takayabu, and D. A. Short (1997), Diurnal variations in tropical oceanic cumulus convection during TOGA COARE, *J. Atmos. Sci.*, *54*, 639–655.
Tompkins, A. M. (2001), Organization of tropical convection in low vertical wind shears: The role of cold pools, *J. Atmos. Sci.*, *58*, 1650–1672.
Vivekanandan, J., S. M. Ellis, R. Oye, D. S. Zrnić, A. V. Ryzhkov, and J. Straka (1999), Cloud microphysics retrieval using S-band dual-polarization radar measurements, *Bull. Am. Meteorol. Soc.*, *80*, 381–388.
Wakimoto, R. M., and N. T. Atkins (1994), Observations of the sea-breeze front during CAPE. Part I: Single-Doppler, satellite, and cloud photogrammetry analysis, *Mon. Weather Rev.*, *122*, 1092–1114.
Weckwerth, T. M. (2000), The effect of small-scale moisture variability on thunderstorm initiation, *Mon. Weather Rev.*, *128*, 4017–4030.
Weckwerth, T. M., J. W. Wilson, and R. M. Wakimoto (1996), Thermodynamic variability within the convective boundary layer due to horizontal convective rolls, *Mon. Weather Rev.*, *124*, 769–784.
Weckwerth, T. M., J. W. Wilson, R. M. Wakimoto, and N. A. Crook (1997), Horizontal convective rolls: Determining the environmental conditions supporting their existence and characteristics, *Mon. Weather Rev.*, *125*, 505–526.
Weckwerth, T. M., T. W. Horst, and J. W. Wilson (1999), An observational study of the evolution of horizontal convective rolls, *Mon. Weather Rev.*, *127*, 2160–2179.
Wilson, J. W., T. M. Weckwerth, J. Vivekanandan, R. M. Wakimoto, and R. W. Russell (1994), Boundary layer clear-air radar echoes: Origin of echoes and accuracy of derived winds, *J. Atmos. Oceanic Technol.*, *11*, 1184–1206.
Xu, W., and S. A. Rutledge (2014), Convective characteristics of the Madden-Julian Oscillation over the central Indian Ocean observed by shipborne radar during DYNAMO, *J. Atmos. Sci.*, *71*, 2859–2877.
Yoneyama, K., C. Zhang, and C. N. Long (2013), Tracking pulses of the Madden-Julian Oscillation, *Bull. Am. Meteorol. Soc.*, *89*, 1871–1891.
Yuter, S. E., and R. A. Houze Jr. (1997), Measurements of raindrop size distributions over the Pacific warm pool and implications for Z-R relations, *J. Appl. Meteorol.*, *36*, 847–867.
Zhang, C. (2005), Madden-Julian Oscillation, *Rev. Geophys.*, *43*, RG2003, doi:10.1029/2004RG000158.
Zipser, E. J. (1969), The role of organized unsaturated convective downdrafts in the structure and rapid decay of an equatorial disturbance, *J. Appl. Meteorol.*, *8*, 799–814.
Zuidema, P., Z. Li, R. J. Hill, L. Bariteau, B. Rilling, C. Fairall, W. A. Brewer, B. Albrecht, and J. Hare (2012), On trade wind cumulus cold pools, *J. Atmos. Sci.*, *69*, 259–280.
Zuluaga, M. D., and R. A. Houze Jr. (2013), Evolution of the population of precipitating convective systems over the equatorial Indian Ocean in active phases of the Madden-Julian Oscillation, *J. Atmos. Sci.*, *70*, 2713–2725.